SH seismoelectric response of a glacier: an analytic study

L. B. Monachesi[1,2] *, F. I. Zyserman[1,3] † and L. Jouniaux[4] ‡

Leonardo B. Monachesi, lmonachesi@unrn.edu.ar

[1]CONICET

[2]Instituto de Investigación en

Paleobiología y Geología, Universidad

Nacional de Río Negro.

[3]Facultad de Ciencias Astronómicas y

Geofísicas, Universidad Nacional de La

Plata.

[4]Institut de Physique du Globe de

Strasbourg, EOST, UdS-CNRS UMR 7516,

Université de Strasbourg.

*Av. Roca 1242, Gral. Roca, Río Negro,

Argentina.

Abstract.

In this work we derive the analytic solutions to the system of equations modeling, within the framework of Pride's theory, the seismic-to-electromagnetic conversions taking place in a glacial environment. Considering a one dimensional approach, we set a pure shear horizontal (SH) wave seismic source on top of an elastic medium representing the glacier, which overlies a porous medium fully-saturated with water, representing the glacier bed. The obtained solutions allow to separately represent and analyze the induced electromagnetic responses, the so called coseismic waves, for both the electric and magnetic fields along with the signals originated at the glacier bottom, the electric interface response and magnetic interface response. We also propose approximate solutions, useful to be used in a fast inversion algorithm. We analyze the characteristics of the induced electromagnetic signals and their dependence on the type of glacier bed, considering an unconsolidated one and a consolidated one. The main results of the present paper are manifold, on the one hand, the mentioned analytic solutions, on the other hand, that the electric interface response originated at the glacier bottom is proportional to the electric current density at this depth, and depends on textural and

---

†Paseo del Bosque s/n, B1900FWA La

Plata, Argentina.

‡5 rue René Descartes, 67084 Strasbourg,

France.

electrical properties of the basement. We also showed that the amplitude of the electric interface response is three orders of magnitude higher than the amplitude of the electric coseismic field. This fact reinforces the idea proposed in our previous works that it would be interesting to test SH seismoelectrics as a possible geophysical prospecting and monitoring tool.

Keypoints:

- We derive both exact and approximate analytic solutions to model the SH seismoelectric response of a glacier system

- The obtained results suggest that SH seismoelectrics could constitute a possible geophysical prospecting tool

1. Introduction

The fact that glaciers and their interaction with the subglacial environment could be successfully studied using electromagnetic methods has been observed several years ago; *Blake and Clarke* [1999] noticed that the chemical evolution of subglacial water could contribute to changes in the electric conductivity of the glacier basement, and that streaming potentials are generated by water flow through the sediments located below the ice mass. *Shean and Marchant* [2010] were able, by means of GPR and seismic surveys in Antarctica, to estimate local ice-thicknesses in both upper Mullins Valley and upper Beacon Valley, while *Palmer et al.* [2013] detected the existence of subglacial lakes in Greenland by means of airborne radio echo sounder measurements. Several other examples of GPR used to investigate glaciers can be found in *Nobes* [2011].

Another motivation for the scientific study of glaciers and ice caps, among many others, is their possible contribution to the sea-level rise [*VanLooy et al.*, 2006; *Larsen et al.*, 2007], which is related to their total volume [*Huss and Farinotti*, 2012; *Grinsted*, 2013]. Large scale surveys are necessary in this case, for which airborne laser altimetry/Lidar and digital elevation models (DEMs) can be counted between the used tools [*VanLooy et al.*, 2006; *Rémy and Parouty*, 2009; *Jordan et al.*, 2016; *Rius et al.*, 2017].

Another electromagnetic method that could be used at a local scale in glacial environments is the seismoelectric method. Seismoelectric conversions can arise at interfaces of media with different physical properties, especially electrokinetic properties [*Haartsen and Pride*, 1997; *Garambois and Dietrich*, 2002]. These properties are linked to the coupling between the water flow and the electrical flow. In the seismoelectric method a seismic

wave source is employed to induce a relative motion between the fluid and the matrix, which in turn induces an electrokinetic coupling at the origin of the seismoelectric conversions. Therefore this method could constitute a prospecting tool for the detection of the interface between the glacier and the underlying water-saturated sediments. *Kulessa et al.* [2006] conducted the first -to the authors' knowledge- seismoelectric field test on a glacier, namely the Tsanfleuron glacier, located in the Swiss Alps. They recorded strong seismoelectric signals, and interpreted them as conversions within the snow pack and near the dry-wet ice and ice-bed interfaces. They also observed that seismoelectric signals in glacial ice were stronger than those measured in other environments, such the ones obtained by *Beamish and Peart* [1998]. *Mahardika* [2013] performed numerical tests simulating the glacial environment described in the previous work, and was able to produce recordings compatible with the data collected by *Kulessa et al.* [2006]. Quite recently, *Siegert et al.* [2018] interpreted, from seismoelectric soundings of the West Greenland Ice Sheet, arrival times from the till layer beneath the ice-sheet base fully compatible with previous data obtained with seismic AVO surveys. They suggested this study strongly encourages future developments of the seismoelectric method for the hydrological and mechanical characterization of ice-sheet substrates.

On the other hand, in the laboratory it was proven that an interface between a frozen sand layer and an unfrozen sand layer can induce a seismoelectric signal called the interfacial response. Using a high frequency P-wave source, *Liu et al.* [2008] observed both the seismoelectric conversion propagating with the seismic wave, with a decreasing amplitude when the temperature increased from -8 to -4 °C, and the interfacial response with an electric field amplitude of the order of 10 mV m^{-1}. The seismoelectric method

has been also used to study different environments, theoretically, in the laboratory and in the field. We mention just some examples among the numerous and valuable works that many authors have produced: studies of shallow seismoelectrics [*Haines et al.*, 2007a, b], the analysis of seismoelectric signals created by fault ruptures [*Hu and Gao*, 2011], the study of seismoelectric effects produced by mesoscopic heterogeneities [*Jougnot et al.*, 2013; *Monachesi et al.*, 2015], the study of hydrological reservoirs [*Dupuis et al.*, 2007; *Dupuis et al.*, 2009; *Schakel et al.*, 2012], hydrocarbon reservoir characterization [*Thompson et al.*, 2005; *Hu et al.*, 2007; *Thompson et al.*, 2007; *Revil and Jardani*, 2010; *Zyserman et al.*, 2010; *Guan et al.*, 2013], CO_2 deposition sites monitoring [*Zyserman et al.*, 2015], partially saturated soils characterization [*Strahser et al.*, 2011; *Warden et al.*, 2013; *Mahardika*, 2013; *Smeulders et al.*, 2014; *Allègre et al.*, 2015; *Jardani and Revil*, 2015; *Bordes et al.*, 2015; *Fiorentino et al.*, 2017; *Zyserman et al.*, 2017a], seismoelectric characterization of layered-earth systems [*Grobbe et al.*, 2016; *Grobbe and Slob*, 2016]. The interested reader can recourse to recent reviews [*Jouniaux and Ishido*, 2012; *Jouniaux and Zyserman*, 2016] and a recent book on seismoelectrics [*Revil et al.*, 2015] for a more extensive list of applications.

With the objective of contributing to characterize and understand the seismoelectric method when applied to glacial environments, we present in this work an analytic study of the electromagnetic responses to pure SH seismic waves, generated by a shearing force acting at the top of a glacier overlying a rocky substratum. Concerning the choice of the source, on the one hand, we have proved in a previous work [*Zyserman et al.*, 2017a] that the signal-to-noise ratio can be higher in this case than when using compressional sources, and on the other hand, although up to now this kind of sources has not been used in seis-

moelectric field studies, they have been employed successfully in several works aiming to characterize the shallow subsurface [*Konstantaki et al.*, 2013, 2015; *Beilecke et al.*, 2016; *Stucchi et al.*, 2017; *Comina et al.*, 2017; *Prior et al.*, 2017]. The ice forming the glacier is treated as an elastic medium; this is a common assumption when performing seismic studies [*Presnov et al.*, 2014a, b; *Collins et al.*, 2016; *Podolskiy and Fabian*, 2016].

Many authors [*Garambois and Dietrich*, 2002; *Hu et al.*, 2007; *Haines et al.*, 2007a, b; *Hu and Gao*, 2011; *Zyserman et al.*, 2012; *Guan et al.*, 2013; *Warden et al.*, 2012, 2013; *Kröger et al.*, 2014; *Bordes et al.*, 2015; *Zyserman et al.*, 2015; *Gao et al.*, 2017; *Guan et al.*, 2017; *Zyserman et al.*, 2017a] have employed Pride's theory [*Pride*, 1994] to model the electrokinetic coupling taking place at the pore walls of an electrolyte saturated rock matrix; in this work we proceed in the same manner to characterize the seismic-to-electromagnetic energy conversions occurring at the glacier bed and at its top border, i.e., at the boundary with the glacier bottom. Moreover, as the glacier beds can be constituted primarily by hard rock [*Payne et al.*, 2004] or by unconsolidated sediments [*Peters et al.*, 2006], we employ two different models for the mechanical properties of the glacier bed, and explore their respective influence on the generated electromagnetic response.

Finally, concerning the interaction of the glacier with its underlying medium, it is modeled by assuming that they move jointly when the shear waves arrive at their common boundary. This assumption is valid for different kind of glaciers, namely the so called "cold-based" or "dry-based" glaciers, i.e., those with their basal part entirely below the pressure melting point, and therefore with no liquid water occurring at the interface between the two media [*Lorrain and Fitzsimons*, 2011], and also for the more erosive "temperate" glaciers, for which thin water sheets or water-filled holes with different shapes can exist

between the glacier bottom and the rocks beneath, allowing the ice to slip and move relatively fast [*Herman et al.*, 2015]. It must be however noticed that in this second case some restrictions involving the frequency content of the signal and the water viscosity, among other parameters, must be taken into account for the "welded" boundary condition to be valid [*Rokhlin and Wang*, 1991]. In summary, we are presenting the first analytic work in which the seismoelectric equations, coupled through appropriate boundary conditions to the elastic equations, are solved and furthermore, the solution is written in a closed form. We follow this work by presenting the governing equations used in this study, and continue by deriving the analytic solutions to the simplified elastic and Pride's equations, considering contributions of infinitely many reflections of the SH seismic wave at the glacier surface and bottom. Further, we consider an approximation to the induced electromagnetic fields, which turns out to produce very simple expressions. Finally, we present the model parameters employed in this study considering different scenarios to explore the responses yielded by the proposed solutions.

2. Theoretical background

2.1. Governing equations

Let's consider a one-dimensional medium constituted by a single layer on top of a half-space in contact at a given depth z_B as it is shown in Fig.1.

The top layer (medium 1) represents the ice body of a glacier, being modeled as an elastic medium, while the half-space (medium 2) is occupied by a porous medium fully-saturated with water, representing the glacier bed. We assume that the seismic source of the system is a shearing force located at the glacier surface ($z = 0$), parallel to the x

axis acting on a horizontal infinite plane. Under these assumptions the source can only induce displacements in the x direction, with amplitudes depending only on depth; no compressional waves can arise in this model; on the other hand, due to the proposed model geometry, spherical spreading and Fresnel zone effects do not take place.

Given that medium 1 is an elastic one, the mechanical equation that governs the wave propagation written in the space-frequency domain, assuming an $e^{i\omega t}$ time dependence, is:

$$-\omega^2 \rho_1 u_x - G_1 \frac{\partial^2 u_x}{\partial z^2} = F^s \delta(z), \tag{1}$$

where ρ_1 and G_1 stand for the density and the shear modulus of medium 1, and u_x is the displacement in the medium [*Aki and Richards*, 2002]. The right hand side of eq. 1 represents the shearing source acting on the surface (F^s is the shearing force per unit area and $\delta(z)$ is the Dirac delta function).

As mentioned above, eq. 1 yields the mechanical response of the considered medium under the stated assumptions. Even though it is not coupled to the electromagnetic response in this region, clearly we have to establish the governing equations for the electric and magnetic fields in the glacier in order to appropriately model the complete response to the seismic wave propagation induced by the source. Because the proposed model is one-dimensional, both the electric and magnetic fields will depend only on depth. Assuming that the net electric charge is zero and that the magnetic permeability is that of the vacuum, the electric and magnetic fields in medium 1 will satisfy the following simplified form of Maxwell's equations:

$$-\sigma_1 E_x - \frac{\partial H_y}{\partial z} = 0, \tag{2}$$

$$\frac{\partial E_x}{\partial z} + i\omega \mu_0 H_y = 0, \tag{3}$$

where E_x and H_y are the electric and magnetic fields, respectively, σ_1 is the electric conductivity of the medium and $\mu_0 = 4\pi \times 10^{-7}$ N A^{-2} is the vacuum magnetic permeability. Note that the displacement currents are not accounted for; this is the common assumption for shallow seismoelectric surveys [*Hu and Liu*, 2002; *Haines and Pride*, 2006; *Bordes et al.*, 2015; *Gao et al.*, 2017; *Guan et al.*, 2017].

To model the seismoelectric response in medium 2 we use the equations derived by *Pride* [1994]. Considering that the electroosmotic feedback can be neglected in Biot's equations, as it is usually assumed for frequencies in the range of interest for shallow seismoelectric surveys (10 Hz to 1 kHz) [*Hu and Liu*, 2002; *Haines and Pride*, 2006; *Warden et al.*, 2013; *Bordes et al.*, 2015; *Guan et al.*, 2017; *Gao et al.*, 2017], Pride's equations can be written as follows:

$$-\omega^2 \rho_b u_{s,x} - \omega^2 \rho_w u_{f,x} - G_2 \frac{\partial^2 u_{s,x}}{\partial z^2} = 0, \tag{4}$$

$$-\omega^2 \rho_w u_{s,x} - \omega^2 g_0 u_{f,x} + i\omega \frac{\eta_w}{\kappa} u_{f,x} = 0, \tag{5}$$

$$-\sigma_2 E_x - \frac{\partial H_y}{\partial z} = i\omega \frac{\eta_w}{\kappa} L_0 u_{f,x} = j_v, \tag{6}$$

$$\frac{\partial E_x}{\partial z} + i\omega \mu_0 H_y = 0, \tag{7}$$

In these equations, $u_{s,x}$ and $u_{f,x}$ are the average solid and relative fluid displacements, respectively, ρ_b is the bulk density, which can be computed as $\rho_b = \rho_s(1 - \phi) + \phi\rho_w$, being ρ_s the density of the solid matrix, ρ_w the density of water and ϕ the porosity of the medium. G_2 is the shear modulus of medium 2, g_0 the Biot's low frequency inertial coupling coefficient, computed as $g_0 = F\rho_w$ [*Santos et al.*, 2004, 2005; *Zyserman et al.*, 2012], where F is the formation factor given by $F = \phi^{-\hat{m}}$, being $\hat{m}$ the cementation exponent, η_w is the water viscosity and κ the permeability of the porous matrix. The

right hand side in eq. 6 is the electric current density, source of the electromagnetic signals, and can be referred to as the viscous current density j_v, whereas $\sigma_2 E_x$ is the conduction current, being σ_2 the electric conductivity of medium 2. The coefficient L_0 is the electrokinetic coupling [$Pride$, 1994]; it creates, in this model, the coupling between the seismic wave and the electric and magnetic fields. If this coupling is zero, there are no seismo-electromagnetic conversions. Within the seismic frequency band it can be written as [$Haines$, 2004]:

$$L_0 = -\frac{\epsilon_w \zeta}{\eta_w F}, \tag{8}$$

where ζ is the zeta potential and ϵ_w is the permittivity of water. In order to solve the problem stated by eqs. 1-7 it is necessary to establish boundary conditions for the displacements and the electromagnetic fields, both in the boundaries of the system ($z = 0$ and $z \to \infty$) and at the interface between both media ($z = z_B$). In the following section the boundary conditions are established and the problem is analytically solved taking advantage of the decoupling of the mechanical and electromagnetic equations; we first solve the mechanical problem, and then, the obtained solution is used to derive the final solutions for the electric and magnetic fields.

3. Derivation of the analytic solution

3.1. Solving the mechanical equations

By solving eq. 1 for $z \geq 0$ assuming a homogeneous half-space, the displacement u_x as a function of z will be given by (see Appendix A):

$$u_x(z) = -\frac{F^s}{i\lambda_1 G_1} e^{i\lambda_1 z}, \tag{9}$$

where

$$\lambda_1 = \omega\sqrt{\frac{\rho_1}{G_1}}. \tag{10}$$

The S-wave phase velocity in medium 1 can be obtained from eq. 10 as $v_1 = \omega/|\lambda_1|$. This wave will travel downwards until it reaches the interface between the glacier and the porous medium, at $z = z_B$. At this point, part of the energy will be reflected from the interface, traveling upwards to the surface, and the rest of the energy will be transmitted to the porous medium beneath the glacier. Let's call $U_x^{R,z_B,(1)}$ the displacement produced by the reflected wave at $z = z_B$ (hereafter, the superscript between brackets indicates a reflection/transmission count). Then, the displacement $u_x(z)$ will be given by the superposition of the incident wave (given by eq. 9) and the mentioned reflection as follows:

$$u_x(z) = -\frac{F^s}{i\lambda_1 G_1}e^{i\lambda_1 z} + U_x^{R,z_B,(1)}e^{-i\lambda_1(z-z_B)}. \tag{11}$$

Note that eq. 11 is also a solution of eq. 1, because the second term verifies the homogeneous equation.

Solving eqs. 4 and 5 (see Appendix B), and denoting by $U_{s,x}^{(1)}$ and $U_{f,x}^{(1)}$ the solid and relative fluid displacements at $z = z_B$ produced by the incident wave (eq. 9), respectively, the solid and relative fluid displacements $u_{s,x}(z)$ and $u_{f,x}(z)$ will be given by:

$$u_{s,x}(z) = U_{s,x}^{(1)}e^{i\lambda_2(z-z_B)} \quad \text{and} \quad u_{f,x}(z) = U_{f,x}^{(1)}e^{i\lambda_2(z-z_B)}, \quad \text{with} \quad U_{f,x}^{(1)} = -\frac{\rho_w}{\left(g_0 - \frac{i\eta_w}{\omega\kappa}\right)}U_{s,x}^{(1)} \tag{12}$$

being λ_2 the wave number of medium 2:

$$\lambda_2 = \omega\sqrt{\frac{1}{G_2}\left(\rho_b - \frac{\rho_w^2}{g_0 - i\eta_w/(\kappa\omega)}\right)}, \tag{13}$$

and $v_2 = \omega/|Re(\lambda_2)|$ its S-wave phase velocity.

In order to find the values for the displacements at $z = z_B$, we assume that the glacier

is welded to the solid matrix of the porous medium. Then, both the displacements u_x and $u_{s,x}$ and the shear stresses $G_1 \frac{du_x}{dz}$ and $G_2 \frac{du_{s,x}}{dz}$ should be continuous at $z = z_B$. From eq. 11 and the solid displacement $u_{s,x}$ given by eq. 12 the continuity conditions for the displacement and the shear stresses for the first incident wave at $z = z_B$ can be respectively stated as follows:

$$-\frac{F^s}{i\lambda_1 G_1}e^{i\lambda_1 z_B} + U_x^{R,z_B,(1)} = U_{s,x}^{(1)}, \tag{14}$$

$$-F^s e^{i\lambda_1 z_B} - i\lambda_1 G_1 U_x^{R,z_B,(1)} = i\lambda_2 G_2 U_{s,x}^{(1)}, \tag{15}$$

from which:

$$U_{s,x}^{(1)} = \frac{2iF^s e^{i\lambda_1 z_B}}{(\lambda_1 G_1 + \lambda_2 G_2)}, \tag{16}$$

$$U_x^{R,z_B,(1)} = \frac{iF^s(\lambda_1 G_1 - \lambda_2 G_2)e^{i\lambda_1 z_B}}{\lambda_1 G_1(\lambda_1 G_1 + \lambda_2 G_2)}. \tag{17}$$

The reflected wave $U_x^{R,z_B,(1)}e^{-i\lambda_1(z-z_B)}$ will travel upwards to the surface, reflecting at this point with the same amplitude (we assume here that the shear stress at the surface is zero, i.e. the shear source is no longer acting). Let's call $U_x^{R,0,(1)}$ the displacement produced by the first reflection at the surface. Then we can write:

$$U_x^{R,0,(1)} = U_x^{R,z_B,(1)}e^{i\lambda_1 z_B} = \frac{iF^s(\lambda_1 G_1 - \lambda_2 G_2)e^{i2\lambda_1 z_B}}{\lambda_1 G_1(\lambda_1 G_1 + \lambda_2 G_2)}. \tag{18}$$

The wave reflected at the surface $U_x^{R,0,(1)}e^{i\lambda_1 z}$ will travel downwards to the interface, and another reflection/transmission will occur. It is possible to prove by induction that the corresponding displacements originated in the n-th reflection/transmission at $z = z_B$ and in the n-th reflection at the surface are given by:

$$U_{s,x}^{(n)} = \frac{2iF^s(\lambda_1 G_1 - \lambda_2 G_2)^{(n-1)}e^{i(2n-1)\lambda_1 z_B}}{(\lambda_1 G_1 + \lambda_2 G_2)^n}, \tag{19}$$

$$U_x^{R,z_B,(n)} = \frac{iF^s(\lambda_1 G_1 - \lambda_2 G_2)^n e^{i(2n-1)\lambda_1 z_B}}{\lambda_1 G_1(\lambda_1 G_1 + \lambda_2 G_2)^n}, \tag{20}$$

$$U_x^{R,0,(n)} = \frac{iF^s(\lambda_1 G_1 - \lambda_2 G_2)^n e^{i2n\lambda_1 z_B}}{\lambda_1 G_1(\lambda_1 G_1 + \lambda_2 G_2)^n}. \tag{21}$$

The relative fluid displacement at $z = z_B$ originated by the n-th transmission can be obtained from eqs. 12 and 19:

$$U_{f,x}^{(n)} = -\frac{\rho_w}{\left(g_0 - \frac{i\eta_w}{\omega\kappa}\right)} \frac{2iF^s(\lambda_1 G_1 - \lambda_2 G_2)^{(n-1)} e^{i(2n-1)\lambda_1 z_B}}{(\lambda_1 G_1 + \lambda_2 G_2)^n}, \tag{22}$$

which allows to write for the relative fluid displacement:

$$u_{f,x}^{(n)}(z) = -\frac{\rho_w}{\left(g_0 - \frac{i\eta_w}{\omega\kappa}\right)} \frac{2iF^s(\lambda_1 G_1 - \lambda_2 G_2)^{(n-1)} e^{i(2n-1)\lambda_1 z_B}}{(\lambda_1 G_1 + \lambda_2 G_2)^n} e^{i\lambda_2(z-z_B)}. \tag{23}$$

Replacing this last expression in the right hand side of eq. 6, the electric current density produced by this displacement can be obtained:

$$\begin{aligned} j_v^{(n)}(z) &= i\omega\frac{\eta_w}{\kappa}L_0 u_{f,x}^{(n)} = \frac{\omega\frac{\eta_w}{\kappa}L_0\rho_w}{\left(g_0 - \frac{i\eta_w}{\omega\kappa}\right)} \frac{2F^s(\lambda_1 G_1 - \lambda_2 G_2)^{(n-1)} e^{i(2n-1)\lambda_1 z_B}}{(\lambda_1 G_1 + \lambda_2 G_2)^n} e^{i\lambda_2(z-z_B)} \\ &= J_v^{(n)} e^{i\lambda_2(z-z_B)}, \end{aligned} \tag{24}$$

where $J_v^{(n)}$ is the electric current density at $z = z_B$ produced by the n-th transmission. Finally, the displacements and the electric current density will be given by the superposition of all the events as follows:

$$u_x(z) = -\frac{F^s}{i\lambda_1 G_1} e^{i\lambda_1 z} + \sum_{n=1}^{\infty} U_x^{R,z_B,(n)} e^{-i\lambda_1(z-z_B)} + \sum_{n=1}^{\infty} U_x^{R,0,(n)} e^{i\lambda_1 z}, \quad 0 \le z \le z_B, \tag{25}$$

$$u_{s,x}(z) = \sum_{n=1}^{\infty} U_{s,x}^{(n)} e^{i\lambda_2(z-z_B)} \quad \text{and} \quad u_{f,x}(z) = \sum_{n=1}^{\infty} U_{f,x}^{(n)} e^{i\lambda_2(z-z_B)}, \quad z \ge z_B, \tag{26}$$

$$j_v(z) = \sum_{n=1}^{\infty} J_v^{(n)} e^{i\lambda_2(z-z_B)}, \quad z \ge z_B, \tag{27}$$

where $U_x^{R,z_B,(n)}$, $U_x^{R,0,(n)}$, $U_{s,x}^{(n)}$, $U_{f,x}^{(n)}$ and $J_v^{(n)}$ are given by eqs. 20, 21, 19, 22 and 24,

respectively.

3.2. Solving the electromagnetic equations

The system of eqs. 2, 3, 6 and 7 can be written in the following equivalent simplified form:

$$\frac{d^2 E_x}{dz^2} + k_1^2 E_x = 0, \qquad 0 \le z \le z_B, \tag{28}$$

$$\frac{d^2 E_x}{dz^2} + k_2^2 E_x = i\omega\mu_0 j_v = i\omega\mu_0 \sum_{n=1}^{\infty} J_v^{(n)} e^{i\lambda_2(z-z_B)}, \quad z \ge z_B, \tag{29}$$

where $k_1 = \sqrt{-i\omega\mu_0\sigma_1}$ and $k_2 = \sqrt{-i\omega\mu_0\sigma_2}$. Note that the source of the electromagnetic fields is given by the electric current density j_v (see eq. 27), and is different from zero only for $z \ge z_B$.

The general solution for eq. 28 is given by:

$$E_x(z) = A_1 e^{-ik_1 z} + B_1 e^{ik_1 z}, \qquad 0 \le z \le z_B, \tag{30}$$

where A_1 and B_1 are complex coefficients. The general solution for eq. 29 can be written as:

$$E_x(z) = A_2 e^{-ik_2 z} + B_2 e^{ik_2 z} - \frac{k_2^2 e^{i\lambda_2(z-z_B)}}{(k_2^2 - \lambda_2^2)\sigma_2} \sum_{n=1}^{\infty} J_v^{(n)}, \quad z \ge z_B. \tag{31}$$

where A_2 and B_2 are complex coefficients and the third term is a particular solution for eq. 29. The magnetic field H_y can be derived from the electric field E_x using eqs. 3 and 7, leading to

$$H_y(z) = \frac{k_1}{\omega\mu_0} A_1 e^{-ik_1 z} - \frac{k_1}{\omega\mu_0} B_1 e^{ik_1 z}, \quad 0 \le z \le z_B, \tag{32}$$

$$H_y(z) = \frac{k_2}{\omega\mu_0} A_2 e^{-ik_2 z} - \frac{k_2}{\omega\mu_0} B_2 e^{ik_2 z} - \frac{i\lambda_2 e^{i\lambda_2(z-z_B)}}{k_2^2 - \lambda_2^2} \sum_{n=1}^{\infty} J_v^{(n)}, \quad z \ge z_B. \tag{33}$$

It is important to remark at this point that both fields are constituted by the superposition of two distinct responses. The first two terms in eqs. 30-33 are perturbations traveling at

velocities given by $\omega/|Re(k_{1,2})|$, that is, the velocity at which the electromagnetic signal travels in the medium. As it is well known, these perturbations are attributed to responses originated at interfaces between two distinct media. The third term in eqs. 31 and 33 can be clearly identified with the coseismic response, traveling at the same velocity $\omega/|Re(\lambda_2)|$ as the solid and fluid displacements.

The unknown coefficients A_1, B_1, A_2 and B_2 should be obtained by imposing conditions at the interface of both media ($z = z_B$), and at the boundaries of the system ($z = 0$ and $z \to \infty$) as it is shown below. First, if we choose k_2 such that $Im(k_2) < 0$, then B_2 must vanish in order to avoid the divergence of the electromagnetic fields when $z \to \infty$. If the Earth's surface is in contact with air, and assuming that the air is an insulator, then the amplitude of the electric field must be constant for $z \leq 0$ in order to avoid its divergence when $z \to -\infty$, and in virtue of eq. 2 $H_y = 0$ for $z < 0$ (see Appendix C). Given that the magnetic field should be continuous at $z = 0$ (see Appendix D), we can write from eq. 32:

$$0 = A_1 - B_1. \tag{34}$$

Both the electric and magnetic fields should be continuous at the interface between the glacier and its basement (see Appendix D). The continuity condition for both fields at $z = z_B$ can be respectively stated, using eqs. 30-33, as follows

$$A_1 e^{-ik_1 z_B} + B_1 e^{ik_1 z_B} = A_2 e^{-ik_2 z_B} - \frac{k_2^2}{(k_2^2 - \lambda_2^2)\sigma_2} \sum_{n=1}^{\infty} J_v^{(n)}, \tag{35}$$

$$\frac{k_1}{\omega\mu_0}(A_1 e^{-ik_1 z_B} - B_1 e^{ik_1 z_B}) = \frac{k_2}{\omega\mu_0} A_2 e^{-ik_2 z_B} - \frac{i\lambda_2}{(k_2^2 - \lambda_2^2)} \sum_{n=1}^{\infty} J_v^{(n)}. \tag{36}$$

The system of eqs. 34-36 completely determine the values for the three complex coefficients A_1, B_1 and A_2:

$$A_1 = B_1 = \frac{k_2^2 (\lambda_2 - k_2)^{-1}}{2 \left[k_1 \sinh(ik_1 z_B) + k_2 \cosh(ik_1 z_B) \right] \sigma_2} \sum_{n=1}^{\infty} J_v^{(n)}, \tag{37}$$

$$A_2 = \frac{k_2^2 \left[k_1 \sinh(ik_1 z_B) - \lambda_2 \cosh(ik_1 z_B) \right] e^{ik_2 z_B}}{(k_2^2 - \lambda_2^2) \left[k_1 \sinh(ik_1 z_B) + k_2 \cosh(ik_1 z_B) \right] \sigma_2} \sum_{n=1}^{\infty} J_v^{(n)}, \tag{38}$$

with which we have the complete solutions for the electric and magnetic fields. Once the fields $E_x(z, \omega)$ and $H_y(z, \omega)$ are known for a given depth z below the surface, the time variation of these fields at that depth is obtained by the inverse Fourier transform. In the following section hypothetical examples are proposed to analyze the electromagnetic responses predicted by the derived analytical solutions.

3.3. Approximate electromagnetic fields

Although the analytic expressions for the fields eqs. 30-33 seem to be quite simple, the involved coefficients A_1, B_1 and A_2 are not. However, under reasonable assumptions it is possible to find a simple approximation to the solution suitable to perform an analysis of the SH seismoelectric response of the proposed model.

Let us consider the ratio $(k_2/\lambda_2)^2$, given by

$$\left(\frac{k_2}{\lambda_2} \right)^2 = \frac{i \mu_0 \sigma_2 G_2}{\rho_b - \frac{\rho_w^2}{g_0 - i\eta_w/(\kappa\omega)}}. \tag{39}$$

We have computed this quotient for a wide range of seismic frequencies in the cases of unconsolidated and consolidated bedrocks considered in this study, yielding values in the order of 1×10^{-5}; so we can safely consider $|k_2/\lambda_2|^2 << 1$. By doing this, it is possible to make some approximations to simplify the expressions of the fields. Neglecting the ratio $(k_2/\lambda_2)^2$ against k_2/λ_2 and assuming that $e^{\pm ik_1 z} \simeq 1$ and $e^{\pm ik_2 z} \simeq 1$, which are very good

approximations for depths not higher than ~ 100 m, then the electric and magnetic fields can be approximated by the following simplified expressions:

$$E_x(z) \simeq \frac{k_2}{\lambda_2 \sigma_2} \sum_{n=1}^{\infty} J_v^{(n)}, \qquad 0 \leq z < \infty, \tag{40}$$

$$H_y(z) \simeq 0, \quad 0 \leq z \leq z_B, \tag{41}$$

$$H_y(z) \simeq \frac{1}{i\lambda_2} \sum_{n=1}^{\infty} J_v^{(n)} - \frac{e^{i\lambda_2(z-z_B)}}{i\lambda_2} \sum_{n=1}^{\infty} J_v^{(n)}, \quad z \geq z_B. \tag{42}$$

Note that these last expressions are simpler than those of the exact solutions, particularly the terms corresponding to the interface response, in which the complex coefficients A_1, B_1 and A_2 are no longer present. The only term in eq. 40 and the first term of eq. 42 constitute the interfacial response for the electric and magnetic fields, respectively, meanwhile the last term in eq. 42 represents the coseismic response.

In the following we analyze the electromagnetic responses predicted by both the exact and the approximate solutions. It is shown that the latter result is a very good approximation to the exact solution, and due to the simplicity of the mathematical expressions of the fields, they are convenient to analyze the SH seismoelectric response of a glacier system.

4. Results and discussion

We describe here the coseismic and interfacial responses of a glacier system induced by the propagation of an SH wave produced by the source acting on the surface. We start by defining the parameters used to model the physical properties of the media, and then we show the displacement and electric current density predicted by the proposed model. Then we compute the coseismic and interfacial signals of both the electric and magnetic

fields. We analyze the amplitude of these electromagnetic conversions, and the effect produced by changes in the properties of the glacier bed. Finally, a comparative analysis of the approximate and exact solutions is performed in order to evaluate the ability of the approximate fields to model the SH seismoelectric response of the glacier system.

4.1. Model parameters

We mentioned in the Introduction that the glacier is assumed to be an elastic medium, therefore, its mechanical description is complete by giving its mass density ρ_1 and shear phase velocity v_1 (from which the shear modulus $G_1 = \rho_1 v_1^2$ can be computed), and is electromagnetically defined by giving its electric conductivity σ_1. This last property depends on temperature, frequency and the presence of mineral impurities, among other variables [*Petrenko and Whitworth*, 1999]. In the present study, following the latter reference, we choose a representative constant real value given in Table 1, where also the values for the previously mentioned employed parameters are listed.

Glacial substrates present diverse morphologies [*Jiskoot*, 2011]. Therefore, as we mentioned in the Introduction, in this work we consider that the glacier bed is either a water saturated poorly consolidated sandstone, or a water saturated consolidated sandstone. This implies, in the context of the modeling scheme described above, the necessity of setting the values of the following parameters (see Table 1): porosity ϕ, solid grains density ρ_s, permeability κ [*Taherian et al.*, 1990; *Yale*, 1984; *Jouniaux and Bordes*, 2012], water density ρ_w and water viscosity η_w. From them other parameters are derived, the already defined bulk density ρ_b and the Biot's low frequency inertial coupling coefficient g_0. For the estimation of the solid matrix shear modulus G_2 in the unconsolidated scenario we use Walton's model [*Mavko et al.*, 2009], appropriate to model this kind of media [*Pride*,

2005; *Bordes et al.*, 2015; *Dupuy et al.*, 2016]:

$$G_2 = \frac{1}{10}\left[\frac{3(1-\phi)^2\hat{C}^2 P}{\pi B^2}\right], \text{ with } B = \frac{1}{4\pi}\left(\frac{1}{G_s} + \frac{1}{G_s + \lambda_c}\right). \tag{43}$$

In this equation, the parameter $\hat{C}$ is the coordination number, related to the packing of the spheres building the solid aggregate, P is the hydrostatic pressure and λ_c is Lamé's coefficient of the effective grain material, and is computed as $\lambda_c = K_s - \frac{2}{3}G_s$, where K_s is the bulk modulus of the solid grains. In this work we consider $\hat{C} = 9$. The hydrostatic pressure can be computed as $P = 101325$ Pa $+ \rho_1 g z_B$. Assuming that the depth of the bottom of the ice body $z_B = 100$ m, the last equation yields $P = 983325$ Pa. Taking for G_s and K_s the values given in Table 1, representative for the shear and bulk moduli of quartz grains, respectively [*Mavko et al.*, 2009], we obtain $G_2 = 0.48$ GPa.

On the other hand, in the consolidated glacier bed scenario, we consider [*Pride*, 2005; *Warden et al.*, 2013; *Solazzi et al.*, 2017]:

$$G_2 = G_s \frac{1-\phi}{1 + \frac{3}{2}c_s\phi}, \tag{44}$$

where $2 < c_s < 20$ is a dimensionless consolidation parameter. As its lower boundary is valid for extremely consolidated rocks, we set in our work $c_s = 8$. With the value for the porosity employed in this case (see Table 1), this model yields $G_2 = 16$ GPa.

To estimate the electric conductivity σ_2 of the glacier bed we use Archie's law:

$$\sigma_2 = \frac{\sigma_w}{F}, \tag{45}$$

where σ_w is the electric conductivity of water. For water containing sodium chloride, σ_w can be computed as $\sigma_w = \sum_{l=Na^+,Cl^-}(ez_l)^2 b_l N_l$, where $e = 1.6 \times 10^{-19}$ C is the electron electric charge, and z_l is the ions' valence, taken to be one for both species. The ions' mobility b_l and concentration N_l (depending on the salinity C_0) are calculated following

Carcione et al. [2003]. For the chosen water salinity, we obtain $\sigma_2 = 1.82 \times 10^{-3}$ S m^{-1}.

Eq. 45 implies that we are considering that the sandstone is a clean one, i.e., it does not contain a significant amount of clay. Had we considered a clayey sandstone, we would have used a corrected version, including the surface conductivity [*Schön*, 1996]. There are several models for the latter, a couple of them are discussed in *Zyserman et al.* [2017b].

4.2. Seismic waves and viscous current density analysis

To illustrate the field responses predicted by the derived analytical solution, we assume as we already mentioned, that the bottom of the glacier is located at $z_B = 100$ m below the surface. For the time signature of the seismic source $f^s(t)$ we use a Ricker wavelet with peak frequency $f_{\text{peak}} = 120$ Hz, the peak amplitude for the Ricker wavelet (located at $t = 8 \times 10^{-3}$ s) is set so that the amplitude of the force per unit area at the surface is equal to 8000 N m^{-2}. This value for the force per unit area can be estimated from the technical data provided for the shear wave generator ELVIS 5.0 [*Krawczyk et al.*, 2013] and assuming that the area of the vibrating plate is 0.0625 m^2 = 0.25 m $\times$ 0.25 m. A similar value for the force per unit area can be computed upon the value of the acceleration produced by a S-wave source generator near the surface, which is around $0.4g$, where g is the gravity acceleration [*Bordes*, 2005]. From eq. 9, recalling that the time dependence is assumed to be $e^{i\omega t}$, for a given angular frequency ω the displacement u_x at the surface ($z = 0$) as a function of time can be written as

$$u_x(0, t) = -\frac{F^s}{i\lambda_1 G_1} e^{i\omega t}, \tag{46}$$

from which, the acceleration of the surface can be obtained

$$\frac{d^2 u_x}{dt^2}(0, t) = \frac{\omega^2 F^s}{i\lambda_1 G_1} e^{i\omega t} = \frac{\omega F^s}{i\sqrt{\rho_1 G_1}} e^{i\omega t}, \tag{47}$$

then, the amplitude of the acceleration will be given by

$$a = \frac{\omega F^s}{\sqrt{\rho_1 G_1}}, \tag{48}$$

from which the force per unit area of the source, F^s, can be obtained

$$F^s = a \frac{\sqrt{\rho_1 G_1}}{\omega}. \tag{49}$$

Replacing the values for ρ_1, G_1, $\omega = 2\pi f_{\text{peak}}$ and $a = 0.4g$ we obtain $F^s = 8422$ N m^{-2}, which is very close to the corresponding value for the ELVIS 5.0 shear wave generator employed in this work.

We point out here that the following analysis is performed considering the unconsolidated scenario; the results for the consolidated case are qualitatively equivalent. The comparative analysis between both scenarios is performed afterwards.

We begin our study by showing the time variation of the solid displacement and the electric current density, plotted in Fig.2 for eleven different depths measured from the surface down to 200 m depth.

The seismic wave travels with a velocity of 1800 m s^{-1} from the surface down to 100 m depth, and with a velocity of 473.4 m s^{-1} below this point, where the interface between the two media is located. There, at the glacier bottom, we can see an upwards traveling reflected wave with a smaller amplitude which arrives at the surface at time 0.12 s. This wave is completely reflected, and travels from the surface downwards to the bottom of the glacier and into the basement. The current density is zero within the glacier because we are modeling the ice as an elastic medium without any fluid content. A current density is induced at the bottom of the glacier at the time 0.06 s corresponding to the arrival of the direct seismic wave at this point, as can be seen in the right panel of this figure.

A second current density, with lower amplitude, is induced by the arrival of the second seismic wave, at about 0.17 s. The third induced current density is barely observable, due to its tiny amplitude, at about 0.28 s in the trace recorded at 100 m depth.

4.3. Coseismic field analysis

The electric and magnetic coseismic fields are shown in the left panels of Figs.3 and 4 respectively. For simplicity, from now on we denote the electric E_x and magnetic H_y fields as E and H, respectively.

The coseismic magnetic field H-Cos is induced by the electric current density. There is no H-Cos neither coseismic electric field E-Cos within the glacier because of the absence of any electric current density. The coseismic magnetic and electric fields propagate at depth supported by the seismic wave: therefore, within the considered temporal window there is a first transmitted coseismic field, a second one related to the first reflected wave at the surface, and a third one related to the second reflected wave at the surface. A plot of the coseismic electric field E-Cos registered at $z = z_B$ is shown in the top-left panel of Fig.5.

The amplitude of the first coseismic event (the one originated when the first incident wave arrives at the interface) is 8 $\times 10^{-3}$ μV m^{-1}. The second and third events have amplitudes of 2 $\times 10^{-3}$ and 0.5 $\times 10^{-3}$ μV m^{-1}, respectively. A plot of the H-Cos field registered at the same depth is shown in the bottom-left panel of Fig.5, being the amplitudes for the first, second and third events of the order of 12.6, 3 and 0.7 μA m^{-1}, respectively.

4.4. Interfacial responses analysis

The electric and magnetic interfacial responses E-IR and H-IR are shown in the right panels of Figs. 3 and 4 respectively. Three events arriving simultaneously at all the receivers can be seen: the first one arriving just before 0.06 s, the second one at 0.17 s and the third at 0.28 s. The former is the first interfacial response originated at the bottom of the glacier, and is produced at the very moment the seismic SH wave hits the bottom of the glacier. The time lapse between the second and the first interface responses corresponds to the lapse employed by the reflected wave to reach the surface and then travel downwards to the bottom of the glacier. Correspondingly, the time lapse between the second and third events coincides with the one between the first and second events. These interfacial responses are related to the jump of the electric current density at the bottom of the glacier (the current density is zero for $z < z_B$ and change abruptly to the value given by eq. 27 for $z \geq z_B$). The E-IR preserves its amplitude above and below the bottom of the glacier, whereas the H-IR shows a large amplitude below this interface and is tiny within the glacier, what makes it to seem absent in the figure. The top-right panel of Fig.5 shows a plot of the E-IR registered at $z = z_B$. The amplitudes for the first, second and third events are 4, 0.92 and 0.2 μV m^{-1} which are three orders of magnitude higher than the corresponding coseismic events. This is a very important feature that could lead to better signal-to-noise ratios when using SH waves seismic sources instead of P wave sources in a seismoelectric survey [*Zyserman et al.*, 2017a, b]. The H-IR is plotted in the bottom right panel of Fig.5. The amplitudes for the three events have amplitudes of 12.5, 2.8 and 0.66 μA m^{-1}. Note that in this case, the amplitudes of the coseismic and interfacial responses are comparable.

Regarding the time signature of both fields, it can be noticed from the figures that the electric coseismic response is markedly different from the corresponding interfacial response, and that both coseismic fields have the same time signature. These features can be explained if we compare the analytical expressions for both the electric and magnetic fields. Note that from the first two terms in eqs. 30-33 the following relation is verified between the magnetic and the electric interface responses

$$H_{IR}(z) = \frac{k_1}{\omega\mu_0} E_{IR}(z), \quad 0 \leq z \leq z_B, \tag{50}$$

$$H_{IR}(z) = \frac{k_2}{\omega\mu_0} E_{IR}(z), \quad z \geq z_B, \tag{51}$$

while from the third terms of eqs. 31 and 33, it can be seen that the coseismic fields verify

$$H_{Cos}(z) = \frac{\lambda_2}{\omega\mu_0} E_{Cos}(z), \quad z \geq z_B. \tag{52}$$

Because the factors $\frac{k_{1,2}}{\omega\mu_0} = \frac{\sqrt{-i\sigma_{1,2}}}{\sqrt{\mu_0}}\omega^{-\frac{1}{2}}$ in eqs. 50 and 51 are frequency-dependent, the frequency spectra of both fields are different, yielding different signatures in the time domain for the electric and magnetic interface responses. On the other hand, the factor $\frac{\lambda_2}{\omega\mu_0}$ in eq. 52, which is also frequency dependent, shows almost no variation with the frequency (at least within the frequency range of the source). Then, the spectra of the electric and magnetic coseismic fields differ only in amplitude so that the time signature of both fields is the same, as it can be seen in the figures.

Note that the time signatures of the coseismic and interface responses are the same but with opposite sign for the magnetic field. This fact can become clear when analyzing the approximate expression of the magnetic field eq. 42, where the amplitudes of both the interfacial (first term) and coseismic (second term) responses at $z = z_B$ are the same and have opposite sign. The behavior for the IRs of both fields confirms the numerical results

we obtained in our previous work [*Zyserman et al.*, 2017a], which were novel because we studied seismoelectric conversions induced by an SH source rather than a compressional wave. In case of a compressional wave source *Warden et al.* [2013]; *Bordes et al.* [2015] and *Peng et al.* [2017] predicted, through numerical modeling and experimental observations, that the IRs have an amplitude that is very small compared to the coseismic one.

4.5. Comparison of unconsolidated and consolidated scenarios

As we have already pointed out, all previous results were obtained considering an unconsolidated glacier bed; we do not show the corresponding ones for the consolidated case because they are qualitatively equivalent. There are, however, differences between both cases that deserve to be displayed and analyzed, task we deal within this section.

One of the most important features of the analytic expressions derived for both the electric and magnetic fields is that they are proportional to the current densities $J_v^{(n)}$ originated at the glacier-basement contact. Therefore, analyzing the behavior of the electric current density variations at $z = z_B$ is relevant in order to understand the behavior of the electromagnetic fields. In Fig. 6 the time variations of the electric current density at the contact between the glacier and its basement are shown for both the unconsolidated and the consolidated scenarios.

Note the markedly different amplitudes between both traces, particularly for the first event, due mainly to the different textural properties of the basements. However, this relation in amplitudes is not translated straightforwardly to the field responses; let us see why. At this depth the amplitude of the solid displacement for the first event is slightly higher in the unconsolidated case, but because of the markedly different porosities and permeabilities of both media, the amplitude of the relative fluid displacement is four orders

of magnitude higher in the unconsolidated case. Moreover, these differences in textural properties lead to an electrokinetic coupling L_0 one order of magnitude higher in the unconsolidated scenario, because of the different porosities and cementation exponents (see eq. 8 and Table 1). However, the hydraulic permeabilities play the most important role in the value of the current density (see eq. 24). These values differ by four orders of magnitude between both glacier beds (see Table 1). As a consequence, although the fluid displacement is four orders of magnitude higher in the unconsolidated case, the different textural properties lead to a different value for the quotient $\frac{L_0}{\kappa}$ that multiplies the fluid displacement in eq. 24. This quotient is three orders of magnitude higher in the consolidated case, giving as a result a difference of approximately a factor 20 between the amplitudes for the current densities, as can be seen in Fig. 6.

Regarding the induced electromagnetic fields, in the top-left panel of Fig.7 we show the time variation for the E-Cos field registered at $z = 120$ m (20 m below the contact) for both cases.

Note that there is a time delay between the events, owed to the markedly different seismic velocities between both basements (473.4 m s^{-1} for the unconsolidated case, and 2594 m s^{-1} for the consolidated case). Moreover, given that, in the consolidated case, the seismic velocity and the shear modulus are higher than the corresponding values for the glacier, there is an inversion of the wavelet when the first reflection occurs (see eq. 17), which in turn implies that the second transmission to the basement will be inverted (see the second event for the E-Cos field in Fig.7). Note that the amplitude decay for consecutive events is higher in the unconsolidated case. This is due to the different incident amplitudes in both cases: In the consolidated case, because of the markedly

different velocities and shear moduli, the amplitude of the first reflected wave is higher than for the unconsolidated case. Then, the amplitude of the second incident wave will be higher for the consolidated case, leading to higher amplitudes for the second transmission. Regarding the amplitude of the E-Cos field for both cases, note that it is higher for the unconsolidated case (at least for the first two events) but still both amplitudes are of the same order of magnitude. This can be explained upon the relative amplitudes of the current density shown in Fig.6. Although the current density is one order of magnitude higher for the unconsolidated case, the factor multiplying the current densities in the third term of eq. 31 is higher in the consolidated case. This is mainly due to the difference in the electric conductivity σ_2, which is one order of magnitude higher in the unconsolidated case. As a consequence, the mentioned factor is lower for the unconsolidated case, and even given that the current density is higher in this case, the E-Cos field turns out to be higher but in the same order of magnitude than in the consolidated scenario.

The time variation of the E-IR response registered at $z = 120$ m is shown in the top-right panel of Fig.7. As was expected, the three events occur at the same time for both cases, given that the glacier properties are the same in both scenarios. Note that for both cases the amplitude of the E-IR field is three orders of magnitude higher than the corresponding amplitude of the E-Cos field.

The corresponding time variation of the magnetic fields are plotted in the bottom panels of Fig.7. As was expected, the H-Cos field (left panel) for both cases show the same time delay than the E-Cos field, and the polarity inversion of the second event is also present in this field. Note, however, that the difference between both amplitudes is higher than in the case of the electric field. This difference comes from the fact that the coefficient

multiplying the current density in the third term of eq. 33 is of the same order in both unconsolidated and consolidated cases (slightly higher in the consolidated case). Then, the amplitude relation between the H-Cos fields for both cases shows almost the same behavior than the amplitude relation for the current densities (see Fig. 6). Correspondingly, the H-IR fields (right panel of Fig.7) show the same amplitude relation than the coseismic fields. Note, finally, that for the magnetic field the amplitudes of both the coseismic field and the interface response field are in the same order of magnitude. This is evident from simple inspection of eq. 42. Note that for depths close to z_B, the factors multiplying the current densities in both terms are in the same order. Remember that the first term in this equation represents the H-IR field, meanwhile the second represents the H-Cos field.

4.6. Comparison between the exact and the approximate fields

With the purpose of evaluating the ability of the approximate fields to model the SH seismoelectric response of the glacier system, we present in this section a comparative analysis between the exact solutions given by eqs. 30-33 and the approximate solutions given by eqs. 40-42. For visualization purposes we limit our analysis to the first events, i.e, the ones originating when the first incident wave impinges the interface between the glacier and its basement. The relative differences between the exact and the approximate fields are independent of the considered event, and as a consequence the same results are obtained if the comparative analysis is performed over the fields originating at the second or third incidences.

From simple inspection of eq. 40 it is clear that no coseismic field is present in the approximated electric field. This is a consequence of the simplifications made in order to derive this expression. The amplitude of the coseismic field given by the exact solutions

(see the third term of eqs. 30 and 31) is in the order of $10^{-3}\mu$V m^{-1}, which is three orders of magnitude lower than the corresponding amplitudes for the E-IR field. For the same reason the H-IR, whose amplitude is in the order of $10^{-3}\mu$A m^{-1} over the glacier-basement contact, is then neglected in the approximate fields, and given that there are no H-Cos field at these depths, then the total magnetic field is approximated by zero, as it is expressed by eq. 41. However, below the contact between the glacier and its basement, H-IR and H-Cos have comparable amplitudes and then, both fields are present in the approximate solutions, as can be observed in eq. 42.

The time variations of both the exact and the approximate E-IR fields corresponding to the first event are plotted in Fig.8 for three different depths: $z = 20$ m (left panel), $z = 120$ m (central panel) and $z = 180$ m (right panel).

Note that for $z = 20$ m the approximate field fits perfectly to the exact solution. This was expected because the approximations made are more precise for smaller depths. The maximum difference between both solutions in this case is in the order of 8 $\times 10^{-3}\mu$V m^{-1}, and given that the maximum amplitude of the E-IR field is 4 μV m^{-1}, then the difference between both solutions turns out to be not bigger than 0.2% of the amplitude of the field. For $z = 120$ m (see central panel in Fig. 8) an appreciable difference can be observed. This was again expected because the approximations loose accuracy for depths from about 100 m and downwards. However, as can be seen from the figure, the time signature of the exact field is preserved by the approximated field, and the only difference lie in the amplitude, being not higher than 6.25% of the amplitude of the field. Finally, as was expected for much larger depths, the approximate solution is not precise for $z = 180$ m (see the right panel of Fig. 8), and the maximum difference between both fields is

about 20% of the total field.

Fig. 9 shows the time variations of the exact and approximate H-IR fields for two depths below the glacier-basement contact: $z = 120$ m (left panel) and $z = 180$ m (right panel).

It is evident that the approximations work better for the lower depth and the maximum amplitude differences are of the same order than the ones depicted for the E-IR at these depths (6.25 % for $z = 120$ m and 20 % for $z = 180$ m).

Although the differences between the exact and the approximate IRs for both fields behave similarly as the depth is increased, this is not the case of the H-Cos field. The approximated H-Cos field (third term in eq. 42) displays a better behavior than the approximated E-IR and H-IR fields, providing a good representation of the exact H-Cos field. Fig. 10 shows the time variation of the exact and approximate H-Cos fields registered at $z = 120$ m (left panel) and $z = 180$ m (right panel).

As can be seen, both solutions fit almost perfectly in both cases, and the maximum amplitude difference is negligible.

The examples given in this section have shown that the approximate solutions work fairly well whenever the depths considered are not higher than 100 m approximately, and with the only restrictions imposed by the assumptions of the model, the approximated expressions for the fields can be safely used to model the SH seismoelectric response of a glacier system. This makes the approximate solutions very useful for one dimensional inversion of the IRs, because they could be used to approximate surface measurements, using very simple expressions to compute the forward model.

5. Conclusions

We have presented an analytic study of the seismoelectric conversions induced by a seismic source generating pure SH waves in a glacier/glacier-bed system, considering a one dimensional problem. More specifically, we set an SH source on the surface of the glacier and modeled the latter as an elastic medium, whilst the glacier bed is represented by a water saturated porous medium. Linking the elastic wave equation with Pride's seismoelectric equations through appropriate boundary conditions at the glacier bottom-glacier bed interface, we were able to analytically compute the induced electromagnetic fields, namely the coseismic magnetic and electric fields, and the interface responses, also for both the electric and magnetic fields. The mentioned fields arise, within the used theoretical frame, due to two different electric currents: one which exists only traveling with the seismic signals and generates the H-Cos field, and another one arising at the boundary between the glacier and its bed when the seismic wave impinges on it. The latter induces the H-IR, which diffuses away from the source at a speed much higher than the one of the seismic wave. The electric fields E-Cos and E-IR are due to the time variation of the respective magnetic fields. We also computed approximations to the obtained solutions, which provide very simple expressions for the electromagnetic fields, and remain valid for depths large enough to enclose all interesting model features. The simplicity of the approximations, in particular the one of the E-IR, makes them appropriate to be employed by a fast one dimensional inversion algorithm, to obtain the glacier bottom depth and other parameters of interest, such as the permeability and electric conductivity, from measurements of the electric field at the surface. We also analyzed the difference in the electromagnetic responses due to different glacier beds,

namely consolidated and unconsolidated ones. We observed that, although the electric current generated at the glacier bottom differs appreciably in both scenarios, the E-IR measured at the surface does not change in the same way, confirming the fact that the interface response is affected by the porosity, permeability, and electric conductivity of the glacier bed. In the considered scenarios, the amplitude relation between the E-IR and E-Cos is similar to what we observed in our previous works, i.e., the former is much stronger than the latter, reinforcing the idea that it would be interesting to test SH seismoelectrics as a possible geophysical tool. Moreover, this setting could take advantage of recent results stating that a multi-electrode array configuration can help to better detect the IR signal [*Devi et al.*, 2015].

Finally, as a closing remark we mention that for the implementation of the seismoelectric method in glacial environments, some issues should be considered. For example, pure shear-wave without any P-wave may be difficult to achieve in the field, although as we mentioned before, shear-wave sources have been successfully employed in several works. Moreover, ice anisotropy and the presence of englacial water pockets and water-filled cracks may complicate the electromagnetic response [*Podolskiy and Fabian*, 2016].

Appendix A: Derivation of the solution to equation 1

Eq. 1 can be written in the following equivalent way:

$$\frac{d^2 u_x}{dz^2} + \lambda_1^2 u_x = -\frac{F^s}{G_1}\delta(z), \tag{A1}$$

where λ_1 is given by eq. 10. Using Laplace Transform, it is easy to show that the solution for $u_x(z)$ is given by:

$$u_x(z) = \left[-\frac{F^s}{\lambda_1 G_1}\sin(\lambda_1 z) + u_x(0)\cos(\lambda_1 z) + \frac{u_x'(0)}{\lambda_1}\sin(\lambda_1 z) \right]\mathcal{H}(z), \tag{A2}$$

where $\mathcal{H}(z)$ is the Heaviside function. Writing the sine and cosine functions in their exponential form and regrouping terms in eq. A2, we obtain:

$$u_x(z) = \left[-\frac{F^s}{2i\lambda_1 G_1} + \frac{u_x(0)}{2} + \frac{u'_x(0)}{2i\lambda_1} \right] e^{i\lambda_1 z} \mathcal{H}(z) + \left[\frac{F^s}{2i\lambda_1 G_1} + \frac{u_x(0)}{2} - \frac{u'_x(0)}{2i\lambda_1} \right] e^{-i\lambda_1 z} \mathcal{H}(z) \tag{A3}$$

Given that λ_1 is a pure real number, and choosing the negative square root of λ_1^2, then, the first term of the last equation represents a wave that travels downwards (remember that the time dependence is chosen to be $e^{i\omega t}$), meanwhile the second one is a wave traveling upwards. If we consider only waves traveling downwards, then, the second term of eq. A3 should vanish:

$$\left[\frac{F^s}{2i\lambda_1 G_1} + \frac{u_x(0)}{2} - \frac{u'_x(0)}{2i\lambda_1} \right] = 0 \tag{A4}$$

Using the last expression in eq. A3 we obtain:

$$u_x(z) = u_x(0)e^{i\lambda_1 z}\mathcal{H}(z). \tag{A5}$$

Now, it remains to determine the value of the constant $u_x(0)$. If we assume that the solid matrix is in perfect contact with the source generator at the surface, then the shear stress applied by the source over the surface F^s should be equal to $\tau_{xz} = -2G_1\epsilon_{xz} = -G_1\frac{\partial u_x}{\partial z}$ (the minus sign indicates that the shear stress is computed taking the normal in the $-z$ direction). Then, taking the first derivative of $u_x(z)$ with respect to z in eq. A5 and evaluating it in $z = 0$ we can write:

$$u'_x(0) = i\lambda_1 u_x(0) = -\frac{F_s}{G_1}, \tag{A6}$$

which leads to the final solution for $u_x(z)$:

$$u_x(z) = -\frac{F^s}{i\lambda_1 G_1} e^{i\lambda_1 z}\mathcal{H}(z). \tag{A7}$$

Eq. A7 shows that the displacement is produced by a shear wave originated at the source position traveling downwards with phase velocity given by $\omega/|\lambda_1|$.

Appendix B: Derivation of the solution to equations 4 and 5

Combining eqs. 4 and 5 the following equation can be written in terms of $u_{s,x}$:

$$\frac{d^2 u_{s,x}}{dz^2} + \lambda_2^2 u_{s,x} = 0, \tag{B1}$$

where λ_2 is given by eq. 13. The general solution for eq. B1 is given by:

$$u_{s,x}(z) = a e^{-i\lambda_2 z} + b e^{i\lambda_2 z}, \tag{B2}$$

being a and b complex constants. Taking λ_2 such that $Re(\lambda_2) < 0$, then the first term in the last equation represents a wave traveling upwards, meanwhile the second one corresponds to a wave traveling downwards. If we consider only waves traveling downwards, then $a = 0$. If we call $U_{s,x}$ the value of the solid displacement at $z = z_B$, then, from eq. B2, $b = U_{s,x} e^{-\lambda_2 z_B}$ and we can write for the solid displacement:

$$u_{s,x}(z) = U_{s,x} e^{i\lambda_2(z - z_B)}. \tag{B3}$$

From eq. 5 we have:

$$u_{f,x}(z) = -\frac{\rho_w}{\left(g_0 - \frac{i\eta_w}{\omega\kappa}\right)} u_{s,x}(z). \tag{B4}$$

Combining eqs. B3 and B4 we obtain:

$$u_{f,x}(z) = U_{f,x} e^{\lambda_2(z - z_B)}, \quad \text{with} \quad U_{f,x} = -\frac{\rho_w}{\left(g_0 - \frac{i\eta_w}{\omega\kappa}\right)} U_{s,x}. \tag{B5}$$

Appendix C: Electric and magnetic fields over the surface

For $z < 0$ (over the surface) we assume that the medium is constituted by air, which is treated as a perfect insulator. Then, both the electric conductivity and the electric

current density will be zero and Maxwell's equations reduce to:

$$\frac{\partial H_y}{\partial z} = 0, \tag{C1}$$

$$\frac{\partial E_x}{\partial z} + i\omega\mu_0 H_y = 0. \tag{C2}$$

From eq.C1 we know that H_y is constant. Then, from eq.(C2). $E_x(z) = az + b$, where a and b are complex constants. However, a must vanish in order to avoid the divergence of the electric field when $z \to -\infty$. Then, E_x is also a constant field, and replacing it in eq.C2 we obtain that $H_y = 0$ for $z < 0$.

Appendix D: Continuity of the electromagnetic fields at $z = 0$ and $z = z_B$

In this appendix we show that both the electric and the magnetic fields should be continuous at the surface and at the glacier bottom. Let's assume a closed rectangular loop crossing the horizontal plane at $z = z_B$, as is depicted in Fig.11.

According to Ampere's Law

$$\oint_{\partial A} \mathbf{H} \cdot \mathbf{dl} = \iint_A \mathbf{j_v} \cdot \mathbf{dA}. \tag{D1}$$

For our model $\mathbf{H} = H_y(z)\ \hat{j}$, $\mathbf{j_v} = j_v(z)\ \hat{i}$ and $\mathbf{dA} = dA\ \hat{i}$, so we can write:

$$\int_{-L/2}^{L/2} H_y(z_B - \Delta z/2)\ dy + \int_{L/2}^{-L/2} H_y(z_B + \Delta z/2)\ dy = \int_{-L/2}^{L/2}\int_{z_B-\Delta z/2}^{z_B+\Delta z/2} j_v(z)\ dzdy. \tag{D2}$$

Integration over y yields

$$H_y(z_B - \Delta z/2) - H_y(z_B + \Delta z/2) = \int_{z_B-\Delta z/2}^{z_B+\Delta z/2} j_v(z)\ dz. \tag{D3}$$

Using the expression for $j_v(z)$ given by eq.27 we have (remember that $j_v(z) = 0$ for $z < z_B$)

$$H_y(z_B - \Delta z/2) - H_y(z_B + \Delta z/2) = \int_{z_B}^{z_B+\Delta z/2} \sum_{n=1}^{\infty} J_v^{(n)} e^{i\lambda_2(z-z_B)} dz, \tag{D4}$$

which gives, after integrating over z

$$H_y(z_B - \Delta z/2) - H_y(z_B + \Delta z/2) = \frac{\sum_{n=1}^{\infty} J_v^{(n)}}{i\lambda_2} \left[e^{i\lambda_2 \Delta z/2} - 1 \right]. \tag{D5}$$

Taking the limit when $\Delta z \to 0$, the right hand side of eq. D5 tends to 0, leading to the following relation:

$$\lim_{z \to z_B^-} H_y(z) = \lim_{z \to z_B^+} H_y(z), \tag{D6}$$

which means that the magnetic field H_y is continuous across the interface between the glacier and its basement. The same reasoning can lead to the following relation valid for the continuity of the magnetic field at the surface

$$\lim_{z \to 0^-} H_y(z) = \lim_{z \to 0^+} H_y(z). \tag{D7}$$

On the other hand, given that the electric field $E_x(z)$ is purely tangential to both the surface and the interface between the glacier and its basement, and the tangential components of the electric field should be continuous across any interface, the same will be valid for the electric field.

References

Aki, K., and P. G. Richards, *Quantitative seismology (2nd Ed.)*, University Science Books, California, 2002.

Allègre, V., L. Jouniaux, F. Lehmann, P. Sailhac, and R. Toussaint, Influence of water pressure dynamics and fluid flow on the streaming-potential response for unsaturated conditions, *Geophysical Prospecting*, *63*, 694–712, doi:10.1111/1365-2478.12206, 2015.

Beamish, D., and R. J. Peart, Electrokinetic geophysics - a review, *Terra Nova*, *10*(1), 48–55, 1998.

Beilecke, T., C. Krawczyk, J. Ziesch, and D. Tanner, Near-surface fault detection using high-resolution shear wave reflection seismics at the CO2CRC Otway Project site, Australia, *J. Geophys. Res.: Solid Earth*, *121*(9), 6510–6532, 2016.

Blake, E., and G. Clarke, Subglacial electrical phenomena, *J. Geoph. Res.: Solid Earth*, *104*(B4), 7481–7495, doi:10.1029/98JB02466, 1999.

Bordes, C., Etude expérimentale des phénomènes transitoires sismo-électromagnétiques: Mise en oeuvre au laboratoire souterrain à bas bruit de rustrel, Ph.D. thesis, Université Joseph Fourier, Grenoble 1, 2005.

Bordes, C., P. Sénéchal, J. Barrière, D. Brito, E. Normandin, and D. Jougnot, Impact of water saturation on seismoelectric transfer functions: a laboratory study of coseismic phenomenon, *Geophys. J. Int.*, *200*, 1317–1335, 2015.

Carcione, J., G. Seriani, and D. Gei, Acoustic and electromagnetic properties of soil saturated with salt water and NAPL, *J. Appl. Geophys.*, *52*, 177–191, 2003.

Collins, J., S. Frank, and A. Metzler, Elastic parabolic equation and normal mode solutions for seismo-acoustic propagation in underwater environments with ice covers, *J. Acoust. Soc. Am.*, *139*, 2672, 2016.

Comina, C., C. Krawczyk, U. Polom, and L. Socco, Integration of SH seismic reflection and Love-wave dispersion data for shear wave velocity determination over quick clays,

Geophys. J. Int., *210*(3), 1922–1931, 2017.

Devi, M., D. Dietrich, and D. Garambois, Sensitivity of seismo-electric waveforms and electric noise to electrode configuration, in *Proceedings of "Near Surface Geoscience 2015" (Turin, Italy)*, p. Mo21P104, EAGE, 2015.

Dupuis, J. C., K. E. Butler, and A. W. Kepic, Seismoelectric imaging of the vadose zone of a sand aquifer, *Geophysics*, *72*, A81–A85, doi:10.1190/1.2773780, 2007.

Dupuis, J. C., K. E. Butler, A. W. Kepic, and B. D. Harris, Anatomy of a seismoelectric conversion: Measurements and conceptual modeling in boreholes penetrating a sandy aquifer, *J. Geophys. Res. Solid Earth*, *114*(B13), B10,306, doi:10.1029/2008JB005939, 2009.

Dupuy, B., S. Garambois, and J. Virieux, Estimation of rock physics properties from seismic attributes - Part 1: Strategy and sensitivity analysis, *Geophysics*, *80*(3), M35–M53, doi:10.1190/GEO2015-0239.1, 2016.

Fiorentino, E., R. Toussaint, and L. Jouniaux, Two-phase lattice boltzmann modelling of streaming potentials: influence of the gas-water interface on the electrokinetic coupling, *Geophys. J. Int.*, *208*, 1139–1156, doi:https://doi.org/10.1093/gji/ggw417, 2017.

Gao, Y., F. Huang, and H. Hu, Comparison of full and quasi-static seismoelectric analytically-based modeling, *J. Geophys. Res.: Solid Earth*, p. doi:10.1002/2017JB014251, 2017.

Garambois, S., and M. Dietrich, Full waveform numerical simulations of seismoelectromagnetic wave conversions in fluid-saturated stratified porous media, *J. Geophys. Res.*, *107*(B7), ESE 5–1, doi:10.1029/2001JB000316, 2002.

Grinsted, A., An estimate of global glacier volume, *The Cryosphere*, *7*(1), 141–151, 2013.

Grobbe, N., and E. Slob, Seismo-electromagnetic thin-bed responses: Natural signal enhancements?, *J. Geophys. Res.*, doi:10.1002/2015JB012381, 2016.

Grobbe, N., E. Slob, and W. Thorbecke, Comparison of eigenvectors for coupled seismo-electromagnetic layered-earth modelling, *Geophys. J. Int.*, doi:10.1093/gji/ggw128, 2016.

Guan, W., H. Hu, and Z. Wang, Permeability inversion from low-frequency seismoelectric logs in fluid-saturated porous formations, *Geophysical Prospecting*, *61*, 120–133, doi: 10.1111/j.1365-2478.2012.01053.x, 2013.

Guan, W., P. Shi, and H. Hu, Contributions of poroelastic-wave potentials to seismo-electromagnetic wavefields and validity of the quasi-static calculation: A view from a borehole model, *Geophys. J. Int.*, , doi:10.1093/gji/ggx417, 2017.

Haartsen, M. W., and S. Pride, Electroseismic waves from point sources in layered media, *J. Geophys. Res.*, *102*, 24,745–24,769, 1997.

Haines, S., Seismoelectric imaging of shallow targets, Ph.D. thesis, Stanford University, 2004.

Haines, S. H., and S. R. Pride, Seismoelectric numerical modeling on a grid., *Geophysics*, *71*(6), 57–65, 2006.

Haines, S. S., A. Guitton, and B. Biondi, Seismoelectric data processing for surface surveys of shallow targets, *Geophysics*, *72*, G1–G8, doi:10.1190/1.2424542, 2007a.

Haines, S. S., S. R. Pride, S. L. Klemperer, and B. Biondi, Seismoelectric imaging of shallow targets, *Geophysics*, *72*, G9–G20, doi:10.1190/1.2428267, 2007b.

Herman, F., T. Adatte, J. Lin, and J. Avouac, Erosion by an Alpine glacer, *Science*, *350*(6257), 192–195, 2015.

Hu, H., and Y. Gao, Electromagnetic field generated by a finite fault due to electrokinetic effect, *J. Geophys. Res.*, *116*, 1132–1143,, 2011.

Hu, H., and J. Liu, Simulation of the converted electric field during acoustoelectric logging, *72nd SEG Annual International Meeting*, *Expanded Abstracts,21* (Salt Lake City, Utah, USA), 348–351, doi:10.1029/2001JB001517, 2002.

Hu, H., W. Guan, and J. Harris, Theoretical simulation of electroacoustic borehole logging in a fluid-saturated porous formation, *J. Acoust. Soc. Am.*, *122*, 135–145, 2007.

Huss, M., and D. Farinotti, Distributed ice thickness and volume of all glaciers around the globe., *J. Geophys. Res.*, *117*(F4), doi: 10.1029/2012JF002,523, 2012.

Jardani, A., and A. Revil, Seismoelectric couplings in a poroelastic material containing two immiscible fluid phases, *Geophys. J. Int.*, *202*(2), 850–870, 2015.

Jiskoot, H., Dynamics of glaciers, in *Encyclopedia of snow, ice and glaciers*, edited by V. Singh, P. Singh, and U. Haritasha, Encyclopedia of Earth Sciences, Springer, 2011.

Jordan, T. M., J. L. Bamber, C. N. Williams, J. D. Paden, M. J. Siegert, P. Huybrechts, O. Gagliardini, and F. Gillet-Chaulet, An ice-sheet-wide framework for englacial attenuation from ice-penetrating radar data, *The Cryosphere*, *10*(4), 1547–1570, doi: 10.5194/tc-10-1547-2016, 2016.

Jougnot, D., J. Rubino, M. R. Carbajal, N. Linde, and K. Holliger, Seismoelectric effects due to mesoscopic heterogeneities, *Geophys. Res. Lett.*, *40*, 2033–2037, doi: 10.1002/grl.50472, 2013.

Jouniaux, L., and C. Bordes, Frequency-Dependent Streaming Potentials: A Review, *Int. J. Geophysics*, *vol.2012* (Hindawi Publishing Corporation), Article ID 648,781, 11 p., doi:10.1155/2012/648781, 2012.

Jouniaux, L., and T. Ishido, Electrokinetics in Earth Sciences: a tutorial, *Int. J. Geophysics*, *vol. 2012*(Hindawi Publishing Corporation), Article ID 286,107, doi: 10.1155/2012/286107, 2012.

Jouniaux, L., and F. Zyserman, A review on electrokinetically induced seismo-electrics, electro-seismics, and seismo-magnetics for Earth sciences, *Solid Earth*, *7*, 249–284, doi: 10.5194/se-7-249-2016, 2016.

Konstantaki, L., D. Draganov, T. Heimovaara, and R. Ghose, Imaging scatterers in land-fills using seismic interferometry, *Geophysics*, *78*(6), EN107–EN116, 2013.

Konstantaki, L., R. Ghose, D. Draganov, G. Diaferia, and T. Heimovaara, Characteriza-tion of a heterogeneous landfill using seismic and electrical resistivity data, *Geophysics*, *80*(1), EN13–EN25, 2015.

Krawczyk, C., U. Polom, and T. Beilecke, Shear-wave reflection seismics as a valuable tool for near-surface urban applications, *The Leading Edge*, *32*(3), 253–263, 2013.

Kröger, B., U. Yaramanci, and A. Kemna, Numerical analysis of seismoelectric wave propagation in spatially confined geological units, *Geophysical Prospecting*, *62*, 133–147, doi:10.1111/1365-2478.12020, 2014.

Kulessa, B., T. Murray, and D. Rippin, Active seismoelectric exploration of glaciers, *Geophys. Res. Lett.*, *33*, L07,503, doi:10.1029/2006GL025758, 2006.

Larsen, C. F., R. J. Motyka, A. A. Arendt, K. A. Echelmeyer, and P. E. Geissler, Glacier changes in southeast Alaska and northwest British Columbia and contribution to sea level rise, *J. Geophys. Res.: Earth Surface*, *112*(F1), 2007.

Liu, Z., L. Yuan, X. Zhang, Z. Liu, and H. Wu, A laboratory seismoelectric measurement for the permafrost model with a frozen-unfrozen interface, *Geophys. Res. Lett.*, *35*,

L21,404, doi:10.1029/2008GL035724, 2008.

Lorrain, R. D., and S. J. Fitzsimons, Cold-based glaciers, in *Encyclopedia of snow, ice and glaciers*, edited by V. Singh, P. Singh, and U. Haritasha, Encyclopedia of Earth Sciences, Springer, 2011.

Mahardika, H., Coupled Hydromechanical and Electromagnetic Responses in Unsaturated Porous Media: Theory, Observation, and Numerical Simulations, Ph.D. thesis, Colorado School of Mines, 2013.

Mavko, G., T. Mukerji, and J. Dvorkin, *The rock physics handbook: Tools for seismic analysis of porous media*, Cambridge University Press, The Pitt Building, Trumpington Street, Cambridge CB2 IRP, United Kingdom, 2009.

Monachesi, L., G. Rubino, M. Rosas-Carbajal, D. Jougnot, N. Linde, B. Quintal, and K. Holliger, An analytical study of seismoelectric signals produced by 1D mesoscopic heterogeneities, *Geophys. J. Int.*, *201*, 329–342, 2015.

Nobes, D., Ground Penetrating Radar measurements over glaciers, in *Encyclopedia of snow, ice and glaciers*, edited by V. Singh, P. Singh, and U. Haritasha, Encyclopedia of Earth Sciences, Springer, 2011.

Palmer, S. J., J. A. Dowdeswell, P. Christoffersen, D. A. Young, D. D. Blankenship, J. S. Greenbaum, T. Benham, J. Bamber, and M. J. Siegert, Greenland subglacial lakes detected by radar, *Geophys. Res. Lett.*, *40*(23), 6154–6159, doi:10.1002/2013GL058383, 2013GL058383, 2013.

Payne, A., A. Vieli, A. Shepherd, D. Wingham, and E. Rignot, Recent dramatic thinning of largest West Antarctic ice stream triggered by oceans, *Geophys. Res. Lett.*, *31*, l23401,doi:10.1029/2004GL021284, 2004.

Peng, R., B. Di, J. Wei, P. Ding, J. Zhao, X. Pan, and Z. Liu, Experimental study of the seismoelectric interface response in wedge and cavity models, *Geophys. J. Int.*, 2017.

Peters, L., S. Anandakrishnan, R. Alley, J. Winberry, D. Voigt, A. Smith, and D. Morse, Subglacial sediments as a control on the onset and location of two Siple Coast ice streams, West Antarctica, *J. Geophys. Res.*, *111*, b01302, doi:10.1029/2005JB003766, 2006.

Petrenko, V., and R. Whitworth, *Physics of Ice*, Clarendon Press, 1999.

Podolskiy, A., and W. Fabian, Cryoseismology, *Reviews of Geophysics*, *54*(4), 708–758, 2016.

Presnov, D., R. Zhostkow, V. Gusev, A. Shurup, and A. Sobisevich, Elastic waves in ice-covered ocean, in *EGU General Assembly Conference Abstracts*, vol. 16, p. 7184, 2014a.

Presnov, D. A., R. A. Zhostkov, V. A. Gusev, and A. S. Shurup, Dispersion dependences of elastic waves in an ice-covered shallow sea, *Acoustical Physics*, *60*, 455–465, doi: 10.1134/S1063771014040150, 2014b.

Pride, S., Governing equations for the coupled electromagnetics and acoustics of porous media, *Phys. Rev. B: Condens. Matter*, *50*, 15,678–15,695, 1994.

Pride, S. R., Relationships between seismic and hydrological properties, in *Hydrogeophysics*, chap. 9, pp. 253–291, Springer, Dordrecht, The Netherlands, 2005.

Prior, D., et al., Initial observations from seismometers frozen into a borehole through the McMurdo Ice Shelf., in *EGU General Assembly Conference Abstracts*, vol. 19, p. 5862, 2017.

Rémy, F., and S. Parouty, Antarctic ice sheet and radar altimetry: A review, *Remote Sensing*, *1*(4), 1212–1239, doi:10.3390/rs1041212, 2009.

Revil, A., and A. Jardani, Seismoelectric response of heavy oil reservoirs: theory and numerical modelling, *Geophys. J. Int.*, *180*, 781–797, doi:10.1111/j.1365-246X.2009.04439.x, 2010.

Revil, A., A. Jardani, P. Sava, and A. Haas, *The Seismoelectric Method: Theory and Application*, Wiley Blackwell, 2015.

Rius, A., E. Cardellach, F. Fabra, W. Li, S. Rib, and M. Hernndez-Pajares, Feasibility of gnss-r ice sheet altimetry in greenland using tds-1, *Remote Sensing*, *9*(7), doi:10.3390/rs9070742, 2017.

Rokhlin, S. I., and Y. J. Wang, Analysis of boundary conditions for elastic wave interaction with an interface between two solids, *J. Acoust. Soc. Am.*, *89*(2), 503–515, 1991.

Santos, J., C. Ravazzoli, P. Gauzellino, J. Carcione, and F. Cavallini, Simulation of waves in poro-viscoelastic rocks saturated by immiscible fluids. numerical evidence of a second slow wave., *J. Comput. Acoust.*, *12*, 1–21, 2004.

Santos, J., C. Ravazzoli, P. Gauzellino, and J. Carcione, Numerical simulation of ultrasonic waves in reservoir rocks with patchy saturation and fractal petrophysicas properties, *Computational Geosciences*, *9*, 1–27, 2005.

Schakel, M., D. Smeulders, E. Slob, and H. Heller, Seismoelectric fluid/porous-medium interface response model and measurements, *Transport in Porous media*, *93*, 271–282, doi:10.1007/s11242-011-9869-8, 2012.

Schön, J., *Physical properties of rocks - fundamentals and principles of petrophysics*, vol. 18, 379-478 pp., Elsevier Science Ltd., Handbook of Geophysical Exploration, Seis-

mic exploration, 1996.

Shean, D., and D. Marchant, Seismic and GPR surveys of Mullins Glacier, McMurdo Dry Valleys, Antarctica: ice thickness, internal structure and implications for surface ridge formation, *J. of Glaciology*, *56*(195), 48–64, 2010.

Siegert, M. J., B. Kulessa, M. Bougamont, P. Christoffersen, K. Key, K. R. Andersen, A. D. Booth, and A. M. Smith, Antarctic subglacial groundwater: a concept paper on its measurement and potential influence on ice flow, *Geological Society, London, Special Publications*, *461*(1), 197–213, doi:10.1144/SP461.8, 2018.

Smeulders, D. M. J., N. Grobbe, H. K. J. Heller, and M. Schakel, Seismoelectric conversion for the detection of porous medium interfaces between wetting and nonwetting fluids, *Vadose Zone J.*, doi:10.2136/vzj2013.06.0106, 2014.

Solazzi, S., L. Guarracino, J. Rubino, T. Müller, and K. Holliger, Modeling forced imbibition processes and the associated seismic attenuation in heterogeneous porous rocks, *J. Geophys. Res.: Solid Earth*, doi:10.1002/2017JB014636, 2017.

Strahser, M., L. Jouniaux, P. Sailhac, P.-D. Matthey, and M. Zillmer, Dependence of seismoelectric amplitudes on water-content, *Geophys. J. Int.*, *187*, 1378–1392, 2011.

Stucchi, E., A. Tognarelli, and A. Ribolini, SH-wave seismic reflection at a landslide (Patigno, NW Italy) integrated with P-wave, *J. Appl. Geophys.*, *146*(Supplement C), 188–197, 2017.

Taherian, M., W. Kenyon, and K. Safinya, Measurement of dielectric response of water-saturated rocks, *Geophysics*, *55*, 1530–1541, 1990.

Thompson, A., J. Sumner, and S. Hornbostel, Electromagnetic-to-seismic conversion: A new direct hydrocarbon indicator, *The Leading Edge*, *26*, 428–435, doi:

10.1190/1.2723205, 2007.

Thompson, A., et al., Field tests of electroseismic hydrocarbon detection, *SEG Technical Program Expanded Abstracts*, pp. 565–568, 2005.

VanLooy, J., R. Forster, and A. Ford, Accelerating thinning of Kenai Peninsula glaciers, Alaska, *Geophys. Res. Lett.*, *33*(21), 2006.

Warden, S., S. Garambois, P. Sailhac, L. Jouniaux, and M. Bano, Curvelet-based seismoelectric data processing, *Geophys. J. Int.*, *190*, 1533–1550, doi:10.1111/j.1365-246X.2012.05587.x, 2012.

Warden, S., S. Garambois, L. Jouniaux, D. Brito, P. Sailhac, and C. Bordes, Seismoelectric wave propagation numerical modeling in partially saturated materials, *Geophys. J. Int.*, *194*, 1498–1513, doi:10.1093/gji/ggt198, 2013.

Yale, D., Network modelling of flow, storage and deformation in porous rocks, *PhD Thesis, Stanford University*, 1984.

Zyserman, F., P. Gauzellino, and J. Santos, Finite element modeling of SHTE and PSVTM electroseismics, *J. Applied Geophysics*, *72*, 79–91, doi:10.1016/j.jappgeo.2010.07.004, 2010.

Zyserman, F., P. Gauzellino, and J. Santos, Numerical evidence of gas hydrate detection by means of electroseismics, *J. Applied Geophysics*, *86*, 98–108, 2012.

Zyserman, F., L. Jouniaux, S. Warden, and S. Garambois, Borehole seismoelectric logging using a shear-wave source:Possible application to CO_2 disposal?, *International Journal of Greenhouse Gas Control*, *33*, 82–102, doi:10.1016/j.ijggc.2014.12.009, 2015.

Zyserman, F., L. Monachesi, and L. Jouniaux, Dependence of shear wave seismoelectrics on soil textures: a numerical study in the vadose zone, *Geophys. J. Int.*, *208*(2), 918–

935, 2017a.

Zyserman, F., L. Monachesi, and L. Jouniaux, Reply to "Comment on "Dependence of shear wave seismoelectrics on soil textures: a numerical study in the vadose zone by F.I. Zyserman, L.B. Monachesi and L. Jouniaux" by Revil, A., *Geophys. J. Int.*, *210*(3), 1652–1658, 2017b.

Table 1. *Values of model parameters used in the present study. Those not shown in this table can be obtained from the present ones using the formulas given in the paper. Values marked with a ⋆ symbol are taken from Collins et al. [2016], those marked with a ‡ symbol are given in Petrenko and Whitworth [1999] and those signaled by a † symbol correspond to sandstone sample S21 in Taherian et al. [1990]. The abbreviations (Unc.) and (Con.) are used for "Unconsolidated" and "Consolidated", respectively. The vacuum permittivity is taken to be $\epsilon_0 = 8.85 \times 10^{-12}$ F m^{-1}.*

| Model parameters			
Ice			
Density, ρ_1 [kg m^{-3}]	$900^\star$	S-wave phase velocity, v_1 [m s^{-1}]	$1800^\star$
Electric conductivity, σ_1 [S m^{-1}]	$10^{-5\ddagger}$		
Glacier bed			
Porosity, ϕ (Unc.)	0.3	Cementation exponent, $\hat{m}$ (Unc.)	1.35
Porosity, ϕ (Con.)	$0.12^\dagger$	Cementation exponent, $\hat{m}$ (Con.)	$2.04^\dagger$
Density of the solid matrix, ρ_s [kg m^{-3}]	2600	Shear modulus, G_s [GPa]	45
Permeability, κ [m^2](Unc.)	10^{-13}	Solid grains bulk modulus, K_s [GPa]	36
Permeability, κ [m^2] (Con.)	$10^{-17\dagger}$	Water viscosity, η_w [Pa s]	1.7×10^{-3}
Water density, ρ_w [kg m^{-3}]	1000	Salinity, C_0 [mol L^{-1}]	5×10^{-3}
Permitivity of water, ϵ_w [F m^{-1}]	80 ϵ_0		
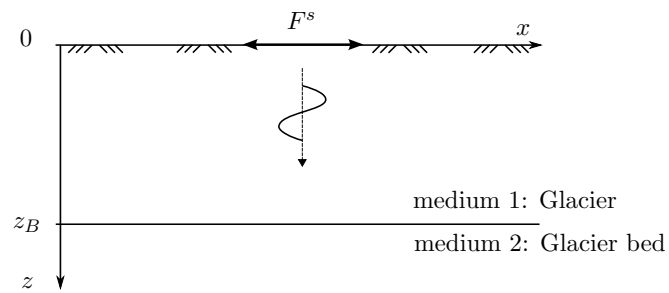
Figure 1. Schematic representation of the seismic shear wave traveling downwards in a two-layer one-dimensional system. Medium 1 represents the ice body (assumed as an elastic medium) and medium 2 is the porous basement (assumed as a poroelastic medium)
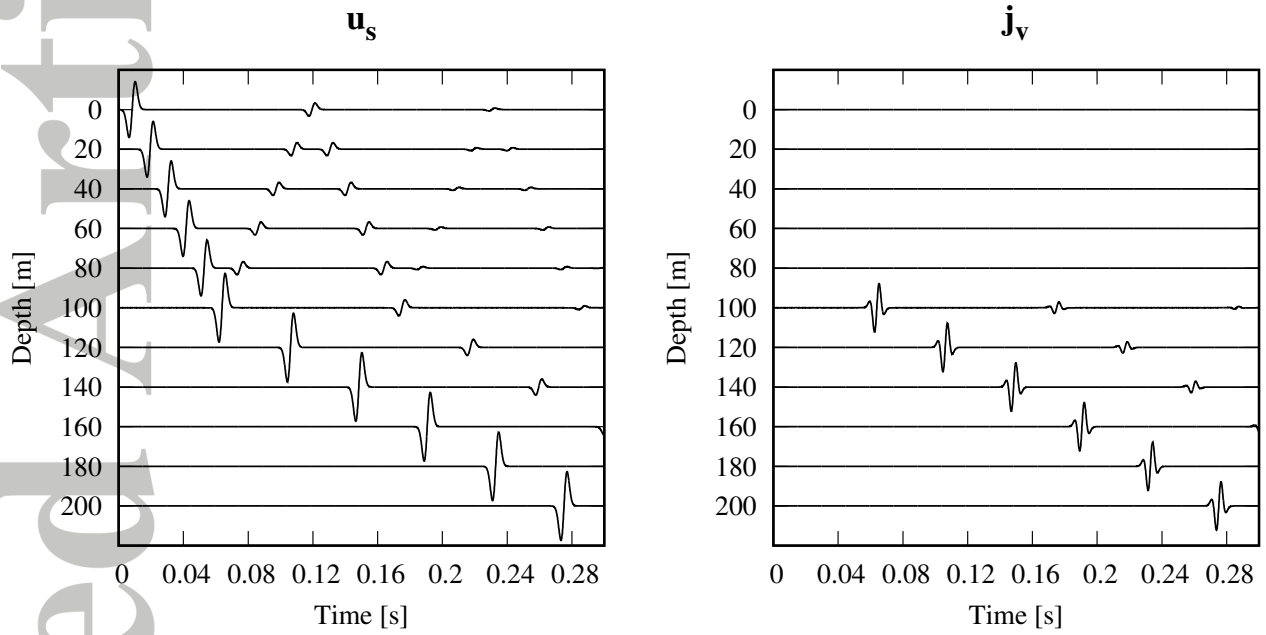
Figure 2. Time variation of the solid displacement (left) and electric current density (right) registered at 11 receivers. The distance between receivers is 20 m. The contact between the glacier and its basement is located 100 m below the surface. In this example the unconsolidated basement case is considered.
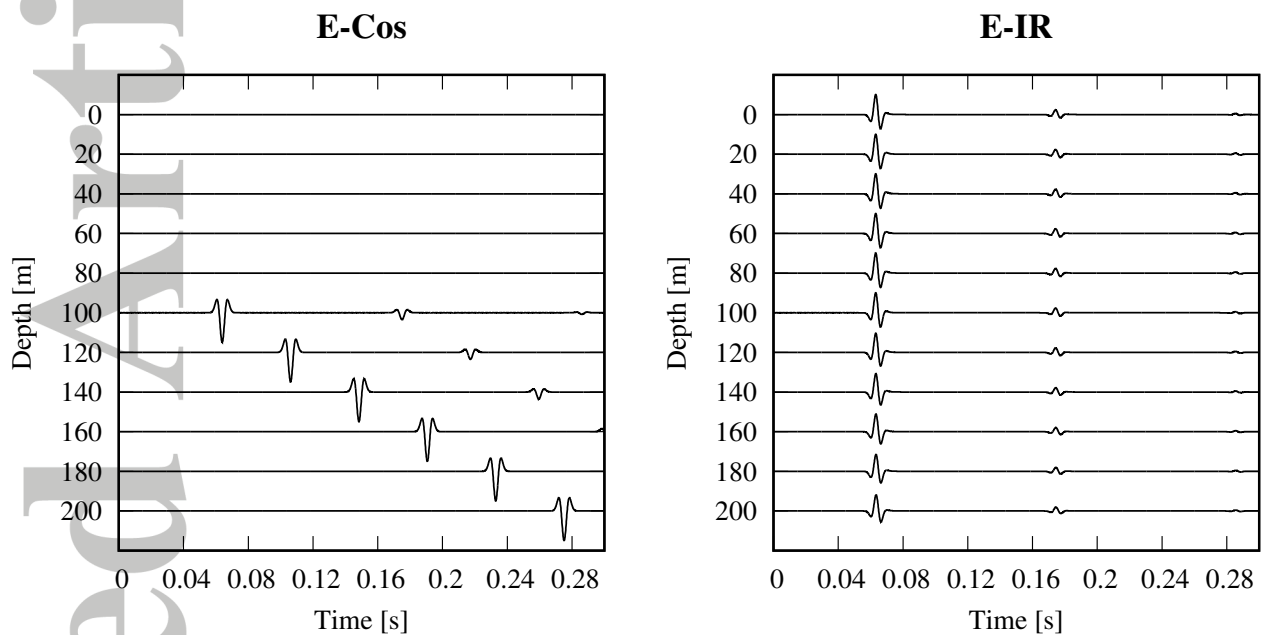
Figure 3. Time variation of the coseismic (left) and interfacial (right) responses for the electric field registered at 11 receivers. The distance between receivers is 20 m. The contact between the glacier and its basement is located 100 m below the surface. In this example the unconsolidated basement case is considered.

H-Cos   **H-IR**
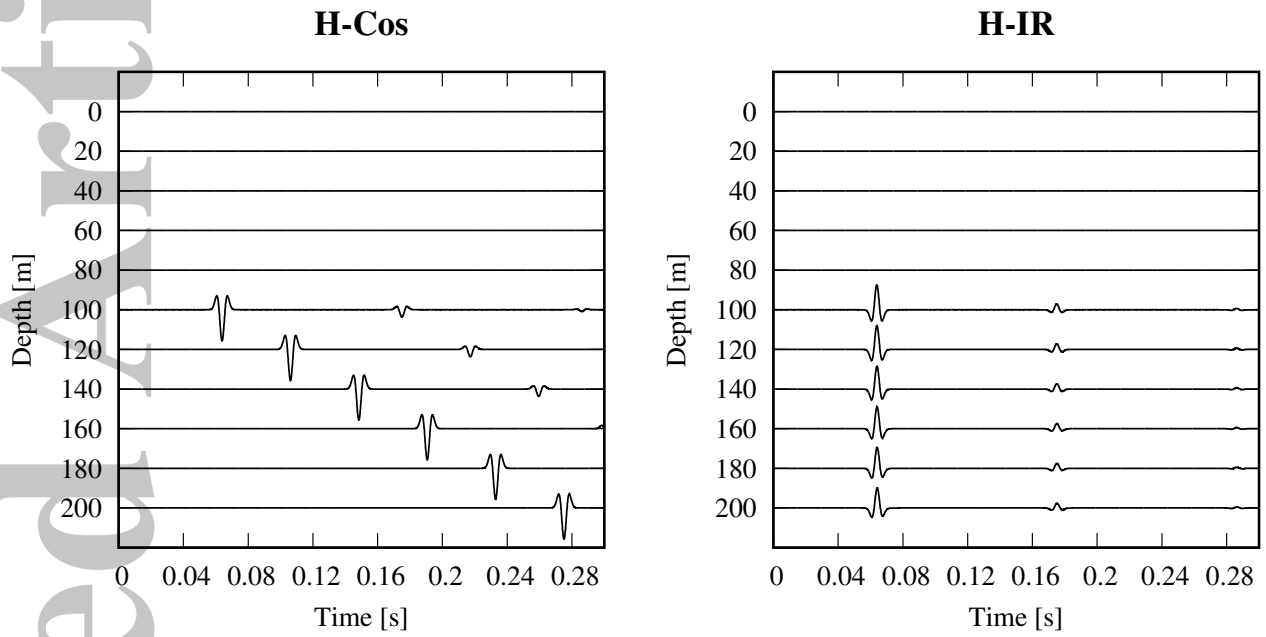
Figure 4.   Time variation of the coseismic (left) and interfacial (right) responses for the magnetic field registered at 11 receivers. The distance between receivers is 20 m. The contact between the glacier and its basement is located 100 m below the surface. In this example the unconsolidated basement case is considered.
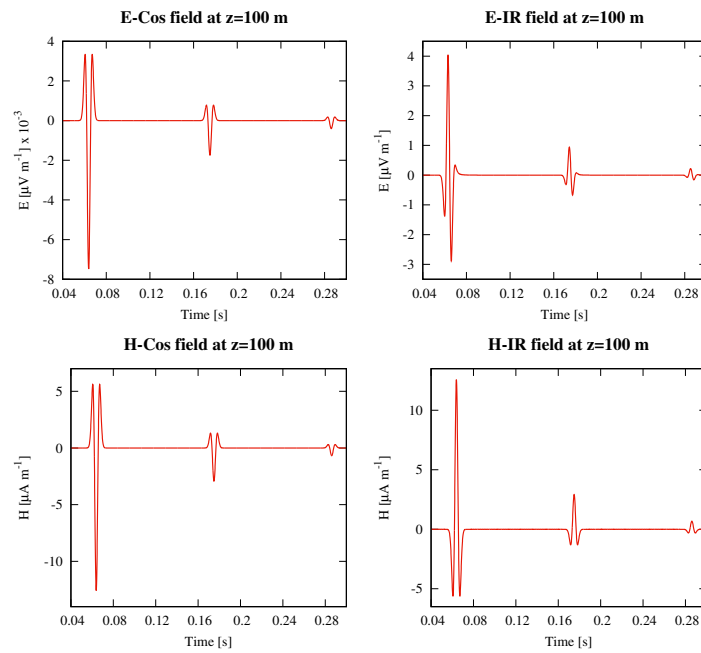
Figure 5. Time variation of the E-Cos (top-left), E-IR (top-right), H-Cos (bottom-left), H-IR (bottom-right) fields registered at $z = 100$ m. In this example the unconsolidated basement case is considered.
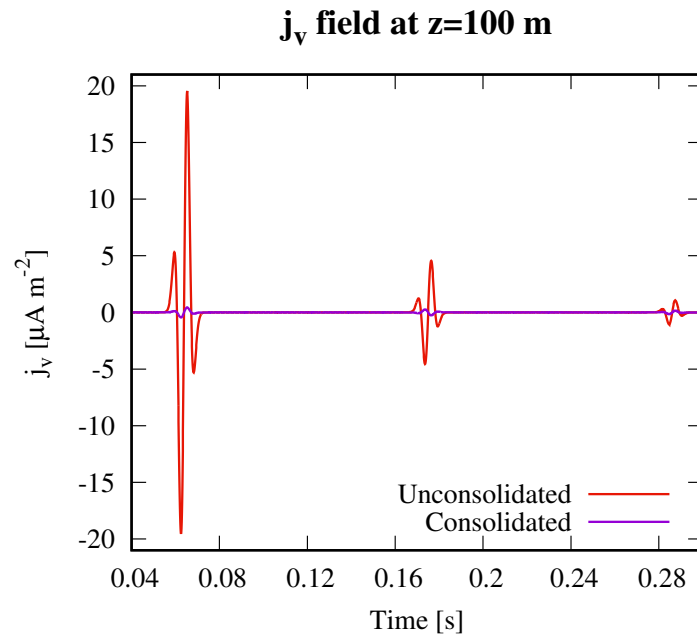
j_v field at z=100 m

Figure 6. Time variation of the electric current density j_v registered at $z = 100$ m for both the unconsolidated and consolidated basement cases.
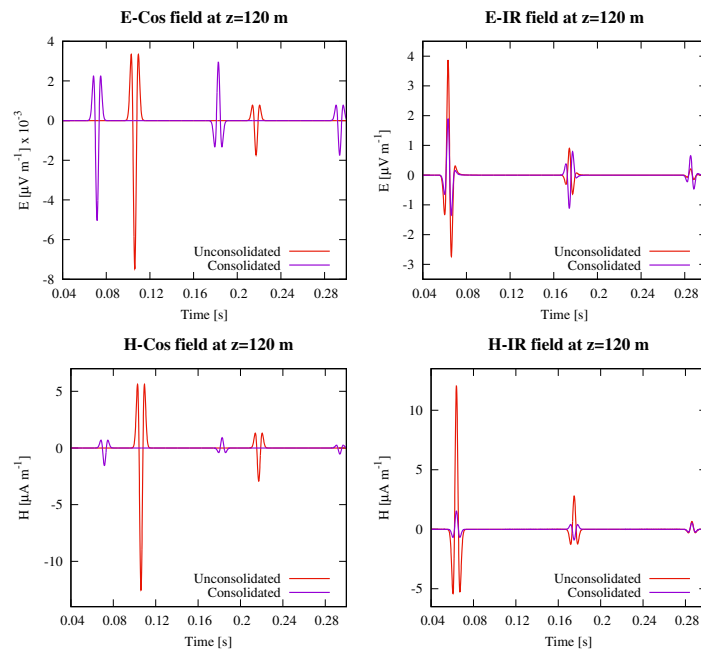
Figure 7. Time variation of the E-Cos (top-left), E-IR (top-right), H-Cos (bottom-left), H-IR (bottom-right) fields registered at $z = 120$ m considering both the unconsolidated and consolidated basement cases.
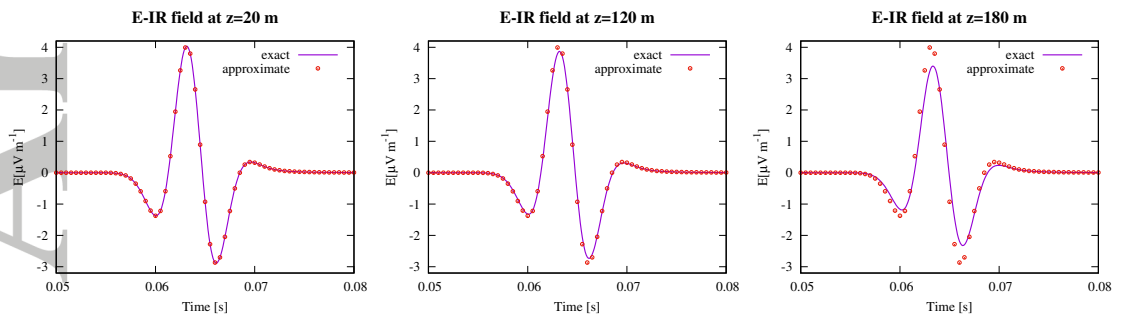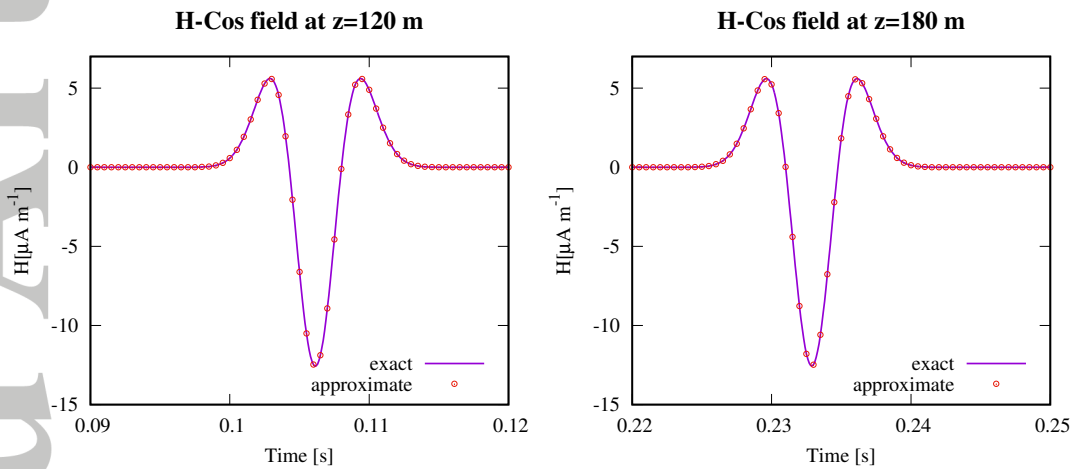
Figure 8. Time variations of the exact and approximate E-IRs for the first event computed at three different depths: $z = 20$ m (left panel), $z = 120$ m (center panel) and $z = 180$ m (right panel). The maximum difference between both the exact and the approximate solutions is 8 $\times 10^{-3} \mu$V m^{-1} at $z = 20$ m, 0.25 μV m^{-1} at $z = 120$ m and 0.8 μV m^{-1} at $z = 180$ m. In this example the unconsolidated basement case is considered.

H-IR field at z=120 m   **H-IR field at z=180 m**
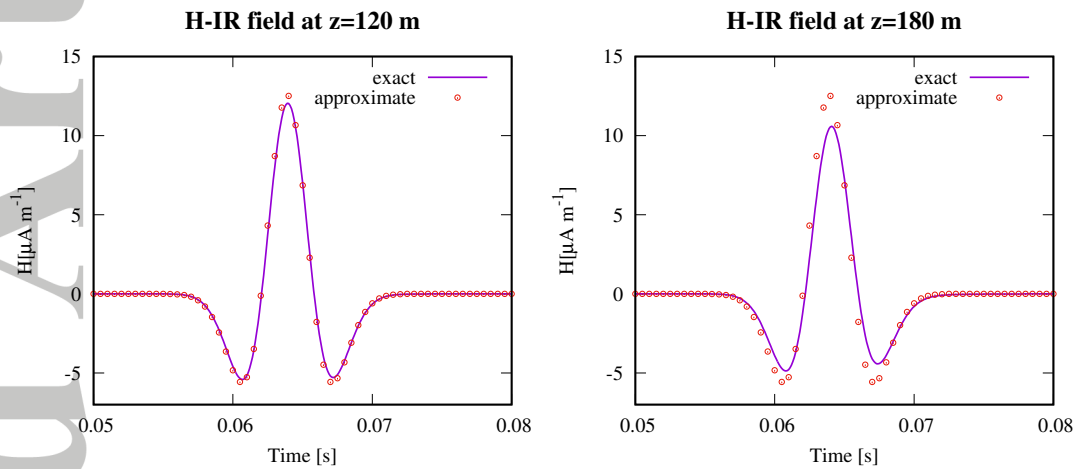
Figure 9. Time variations of the exact and approximate H-IRs for the first event computed at two different depths: $z = 120$ m (left panel) and $z = 180$ m (right panel). The maximum difference between both the exact and the approximate solutions is 0.7 μA m^{-1} at $z = 120$ m and 2.75 μA m^{-1} at $z = 180$ m. In this example the unconsolidated basement case is considered.

Figure 10. Time variations of the exact and approximate H-Cos fields for the first event computed at two different depths: $z = 120$ m (left panel) and $z = 180$ m (right panel). The maximum difference between both the exact and the approximate solutions is in the order of 1 $\times 10^{-17} \mu$A m^{-1} for both depths. In this example the unconsolidated basement case is considered.
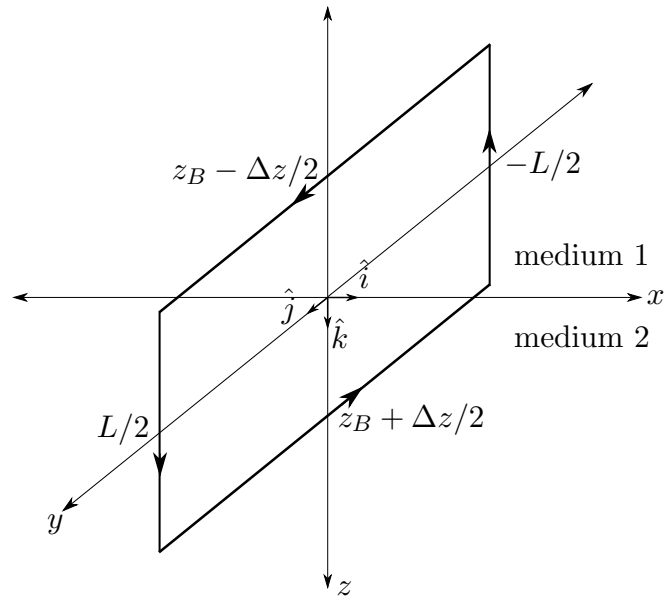
Figure 11. Continuity of H_y at $z = z_B$ - Ampere's Law.